A TRMM rainfall estimation method applicable to land areas

C. Prabhakara[1], R. Iacovazzi Jr.[2],

R. Oki[3] and J. A. Weinman[1]

[1]Goddard Space Flight Center, Greenbelt, Maryland

[2]Raytheon ITSS Corporation

[3]Center for Climate Systems Research, University of Tokyo, Japan

Corresponding Author Address

C. Prabhakara

NASA/Goddard Space Flight Center, Code 913

Greenbelt, Maryland 20771

Phone : 301-286-5390; Fax : 301-286-1759; E- mail : cuddapah@climate.gsfc.nasa.gov

Abstract

Utilizing multi-spectral, dual-polarization Special Sensor Microwave Imager (SSM/I) radiometer measurements, we have developed in this study a method to retrieve average rain rate, R_{f_R}, in a mesoscale grid box of $2^{o} \times 3^{o}$ over land. The key parameter of this method is the fractional rain area, f_R, in that grid box, which is determined with the help of a threshold on the 85 GHz scattering depression deduced from the SSM/I data. In order to demonstrate the usefulness of this method, nine-months of R_{f_R} are retrieved from SSM/I data over three grid boxes in the Northeastern United States. These retrievals are then compared with the corresponding ground-truth-average rain rate, R_g, deduced from 15-minute rain gauges. Based on nine months of rain rate retrievals over three grid boxes, we find that R_{f_R} can explain about 64 % of the variance contained in R_g. A similar evaluation of the grid-box-average rain rates R_{GSCAT} and R_{SRL}, given by the NASA/GSCAT and NOAA/SRL rain retrieval algorithms, is performed. This evaluation reveals that R_{GSCAT} and R_{SRL} can explain only about 42 % of the variance contained in R_g.

In our method, a threshold on the 85 GHz scattering depression is used primarily to determine the fractional rain area in a mesoscale grid box. Quantitative information pertaining to the 85 GHz scattering depression in the grid box is disregarded. In the NASA/GSCAT and NOAA/SRL methods on the other hand, this quantitative information is included. Based on the performance of all three methods, we infer that the magnitude of the scattering depression is a poor indicator of rain rate. Furthermore, from maps based on the observations made by SSM/I on land and ocean we find that there is a significant redundancy in the information

content of the SSM/I multi-spectral observations. This leads us to infer that observations of SSM/I at 19 and 37 GHz add only marginal information to that given by 85 GHz scattering depression.

As with other methods, the area-average rain retrieval method developed in this study needs tuning with radar and/or rain gauge observations. In the TRMM mission, the microwave radiometer rain retrieval algorithm can be tuned with TRMM radar observations. Since the radiometer has about 3.5 times wider spatial coverage compared to the radar in the TRMM mission, such an algorithm can be useful to extend geographically the rain information provided by the TRMM Precipitation Radar.

1. Introduction

In recent studies, rain rates retrieved from the Advance Microwave Precipitation Radiometer (AMPR) on a footprint scale using theoretical models (Heymsfield et al., 1996 and McGaughey and Zipser, 1996) showed poor agreement with radar rain observations made from aircraft. These radiometer and radar observations had a field of view (fov) of a few kilometers. Such poor agreement is also observed in the rain rates deduced theoretically from Special Sensor Microwave Imager[1] (SSM/I) radiometer observations that have a much larger footprint (~ 15 km). During the Global Precipitation Comparison Project (GPCP), SSM/I rain retrievals on a footprint scale were deduced from several algorithms and compared with ship-borne radar rain observations in the TOGA-COARE[2] experiment. Ebert et al. (1996) presented a detailed account of these comparisons. From that GPCP study, we infer that rain rate deduced from the algorithms on a footprint scale over the TOGA-COARE region from the SSM/I radiometer brightness temperatures (T_bs) have only moderate agreement with rain observations made by the ship-borne radars. In addition, these results indicate that mean rain rate deduced from these algorithms, representing averages for all the rain events observed by SSM/I over a time period of about 30 days (time span of a TOGA-COARE ship cruise) and over an

---

[1] *Radiometer of the Defense Meteorological Satellite Program (DMSP) that has 19, 37 and 85 GHz channels in dual polarization and a 22 GHz channel in vertical polarization. This radiometer observes the earth's surface and atmosphere in a conical scan with an incidence angle of ~ 50°. (for more details see Hollinger et al., 1985)*

[2] *Tropical Ocean Global Atmosphere - Coupled Ocean Atmosphere Response Experiment*

1

area of about 300x300 km² (the TOGA-COARE radar scan area) can differ systematically with respect to radar data. Because of such systematic errors, there can be an underestimation of 50 % in one month and an overestimation of 50 % in another month. Based on these findings, Prabhakara et al. (1998) conclude that the measurements made by the microwave radiometer do not contain sufficient information to retrieve good quality rain rates on a footprint scale. This conclusion is consistent with that of an earlier study by Schols et al. (1995).

Rain retrieval on a footprint scale with microwave radiometers over the land is complicated further by terrain, vegetation, and surface wetness. The NASA/GSCAT method of Adler et al. (1994), and the NOAA/SRL algorithm based on the work of Grody (1991) and Ferraro et al. (1995), are designed to estimate rain rate on a footprint scale over land. These methods are rooted in the concepts provided by theoretical models (see for eg. Wu and Weinman, 1984; Kummerow et al., 1989 and Smith and Mugnai, 1992). The GSCAT method works primarily on the premise that rain rate increases as 85 GHz brightness temperature decreases, due to scattering by ice particles. The NOAA/SRL method is analogous, except it incorporates more of the data from the lower frequency channels to screen surface contamination.

In a recent study, Conner and Petty (1998) find that the NASA/GSCAT and NOAA/SRL methods have limited success in retrieving rain information on a footprint scale over land. Furthermore, they show that these methods yield the highest Heidke skill score for detecting rain when the threshold on the rain rate is small (~1 mmhr⁻¹). That skill score decreases as the threshold rain rate increases. They find that the correlation coefficient between rain rate deduced from radar and

2

that retrieved from these methods on a footprint scale using the SSM/I data for a period of nine months over geographic areas of about 3°x3° is about 0.55.

The microwave radiometer observations represent a vertical integral of the information about hydrometeors contained in a column of the atmosphere. Thus, the information about rain contained in the radiometer data is coupled in a non-linear way to that of cloud liquid water, and frozen and melting ice particles of different sizes, shapes, and densities (Schols et al., 1995 and Meneghini, 1996). Multi-channel, dual-polarization measurements of the microwave radiometer have a significant amount of redundant information (Prabhakara et al., 1992 and McGaughey and Zipser, 1996). Hence, the meager amount of independent information contained in the radiometer data cannot resolve all hydrometeors and their vertical distributions. For this reason, in the rain retrieval theoretical models the vertical profiles of hydrometeors above the cloud base are assumed. In particular these models assume that the density and particle size of frozen hydometeors are correlated with the rain rate produced by the clouds. A recent study of Houze (1997), based on aircraft Doppler radar observations of hydrometeors and winds in the TOGA-COARE experiment, indicates that this assumption is not true. This weakness of the algorithms resulting from the limited information content of the microwave radiometer leads to a poor quality of the rain rates deduced on a footprint scale.

In this study, we assume that the amount of ice of all types in clouds is at a minimum and rain rate is near zero in a given pixel when the 85 GHz scattering depression indicated by the SSM/I data has a value near a threshold. Utilizing this threshold on the 85 GHz scattering, we can determine the fractional area enclosed by rain in a mesoscale region. Then, we have developed a rain rate retrieval technique

3

applicable to a mesoscale region that utilizes exclusively this fractional rain area. Thus, this method does not use the complete quantitative information of the 85 GHz scattering depression on a footprint scale.

We may remark that radar with its vertical resolving capability offers distinct advantages over the radiometer. Furthermore, radar back scatter measurements have a d^6 dependence on the rain drop diameter (Battan, 1973), while the radiometer observations tend to have about d^3 dependence (Olson, 1996). For these reasons, we contend radar data can provide good measurements of rain when suitably calibrated with surface rain gauges. However, the radar in the TRMM[3] mission has less than a third of the scanning capability of the microwave radiometer (Simpson et al., 1996). This much larger scanning capability of the radiometer could be exploited to give more temporal and spatial coverage of rain information. However, we need a mesoscale rain retrieval technique based on the radiometer data that can be tuned with a limited amount of ground-truth radar observations. Such a method was developed for the SSM/I data on ocean (Prabhakara et al., 1998). The aim of this study is to develop this type of method for the land.

2. Information about rain contained in the SSM/I data

In order to understand in detail the relationship between the microwave radiometer T_b and observed rain rate, we make comparisons of the spatial distributions of brightness temperature in the 85 GHz horizontal polarization channel T_{85h} and observations of rain rate for two mesoscale rain events. We are presenting one such comparison over ocean, and another over land to illustrate the

---

[3]*Tropical Rainfall Measuring Mission (see Simpson et al., 1996)..*

similarities in the microwave radiometer information over these regions. Because of the relatively small footprint size (~ 15 km) and strong extinction, the brightness temperatures in the 85 GHz channel are emphasized in these comparisons.

Over the ocean, a rain event is chosen from the TOGA-COARE experiment, where observations of rain rate are made by ship-borne radars. These radars were calibrated with rain gauges on buoys and ships (Short et al., 1997). The SSM/I data are matched with the radar data to within the time taken to complete a radar volume scan, i.e., 10 minutes. Furthermore, spatial matching between the two sets of data is within a few kilometers.

As a land case, we have chosen a Mesoscale Convective System (MCS) event that occurred over the Northeastern United States in a $2^{\circ} \times 3^{\circ}$ grid box centered close to $79^{\circ}W$ and $40^{\circ}N$ (the state of Pennsylvania). The distribution of observed rain rate on land in our study is obtained from 15-minute rain gauge data. About 83 % of these rain gauges over the United States are Fisher-Porter (FP) rain gauges. These rain gauges have a poor sensitivity and can indicate only 15-minute accumulation of rain in increments of 0.1 in. In the remaining gauges, 15-minute accumulation of rain is measured in increments of 0.01 in. For uniformity in this study, these rain rates are converted to $mmhr^{-1}$, and then rounded to the nearest unit. We find observations from about 40 rain gauges in a grid box of $2^{\circ} \times 3^{\circ}$ can lead to a representative average in that box. Such a density of gauges is present in some of the Northeastern United States. This density decreases in the Midwest, and is poor (~ 5 gauges per $2^{\circ} \times 3^{\circ}$ grid box) in the Western states. For this reason, this study of precipitation on land is limited to a small section of the Northeastern United States, where there is a dense network of rain gauges.

The observations made by surface radars on land were not considered in our study. As pointed out by Conner and Petty (1998), these radar data have significant problems such as ground clutter, beam spreading, blockage by structures and topography, bright band, and anomalous propagation. They infer that because of several problems, surface radars can underestimate rain rate by as much as a factor of five. Hence, the data from rain gauges are commonly used to adjust the radar measurements (see for e.g. Oki et al., 1997).

In Figure 1a, we show a map of T_{85h} over the TOGA-COARE region for a rain event that occurred at 1031 UTC on 24 Dec. '92 (Day 359). A rain rate map deduced from the ship-borne radars corresponding to this event is shown in Figure 1b. Some regions with intense rain rate (> 4 mmhr^{-1}) are identified in Figure 1b with light shading; while other such intense rain regions are identified with cross hatching. This differentiation is done on the basis of the information given in the map of T_{85h} presented in Figure 1a. Generally, the light-shaded areas correspond to regions where T_{85h} is relatively warm (~ 260 K); while the cross-hatched areas correspond to regions where T_{85h} is cold (< 200 K).

In Figure 1c, a scatter plot of radar rain rate versus radiometer T_{85h} is shown to summarize the characteristics of the rain rates described above. We observe from this figure one maximum in the rain rate when T_{85h} is approximately 260 K, and another maximum when T_{85h} is around 200 K. These intense rain rates associated with relatively warm (cold) T_{85h} are referred to as "warm" ("cold") convective rain. Only a few footprints show intense rain, while a large number near 260 K or 200 K show rain rates that are weak (approaching near zero value). These weak rain rates are broadly referred to as stratiform rain. From Figure 1c, we note that weak rain rates can be present for all possible values of T_{85h}.

6

T_{85h} (K)

a

RADAR RAIN RATE (mmhr^{-1})

b

LATITUDE S

LONGITUDE E

LATITUDE S

LONGITUDE E

T_{37h} (K)

d

LATITUDE S

LONGITUDE E

Radar Rain Rate vs. T_{85h}

c)

Radar Rain Rate (mmhr^{-1})

T_{85h} (K)

Radar Rain Rate vs. T_{37h}

e)

Radar Rain Rate (mmhr^{-1})

T_{37h} (K)

Figure 1: Maps of a) SSM/I T$_{85h}$ and b) the coincident radar rain rate data in the TOGA-COARE region for 24 Dec. '92 at 1031 UTC. In 1b, regions with intense rain rate (> 4 mmhr^{-1}) are identified with light shading and cross hatching. This differentiation is done on the basis of the information given in the map of T$_{85h}$ presented in 1a. Light-shaded areas correspond to regions where T$_{85h}$ is relatively warm (~ 260 K); while the cross-hatched areas correspond to regions where T$_{85h}$ is cold (< 200 K). c) Scatter plot of coincident 85 GHz SSM/I radiometer brightness temperature (K) measurements and radar rain observations (mmhr^{-1}) over the TOGA-COARE region. d) Map of SSM/I T$_{37h}$ in the TOGA-COARE region for 24 Dec. '92 at 1031 UTC. e) Scatter plot of coincident 37 GHz SSM/I radiometer brightness temperature (K) measurements and radar rain observations (mmhr^{-1}) over the TOGA-COARE region.

In Fig 1d a map of the 37 GHz SSM/I data corresponding to the above TOGA-COARE rain event is shown to illustrate the redundancy in the information conveyed by the 85 and 37 GHz channels. In several large areas (> 50x50 km^2), where the 85 GHz channel shows a significant depression, the 37 GHz channel shows a noticeable warming. Furthermore, the scatter plot shown in Figure 1e of T_{37h} versus rain rate for this event indicates that near zero rain rate (averaged over the 37 GHz footprint) can be present at all possible values of T_{37h}. This property of T_{37h} is similar to that of T_{85h} shown in Figure 1c. Thus, we find from these observations that estimation of rain rate for given values of T_{85h} and/or T_{37h} can be totally non-representative of the ground-truth rain rate. This is also true of the 19 and 22 GHz channels.

In Figures 2a, b, c, and d, we are presenting information pertaining to an MCS event that took place over the Northeastern United States in a $2^o \times 3^o$ grid box centered close to $79^o W$ and $40^o N$. This event happened at 619 EST on 22 Aug. '87. In Figure 2a, we present an analysis of T_{85h} data that is similar to that in Figure 1a. In Figure 2b, we present the distribution of rain rate on land for this event using the available data from rain gauges. We may emphasize that the heavily shaded area of Figure 2a, where strong 85 GHz scattering is observed (T_{85h} < 200 K), is at least 50x100 km^2. Although this is the region with the heaviest scattering, the maximum rain intensity of 30 mmhr^{-1} is observed 50 km away in a region where T_{85h} is about 240 K. Furthermore, rain intensity varies somewhat randomly from 0 to 10 mmhr^{-1} over the area encompassed by the 230 K contour of T_{85h}. We infer from these two figures that the rain rate on land does not necessarily increase as T_{85h} decreases.
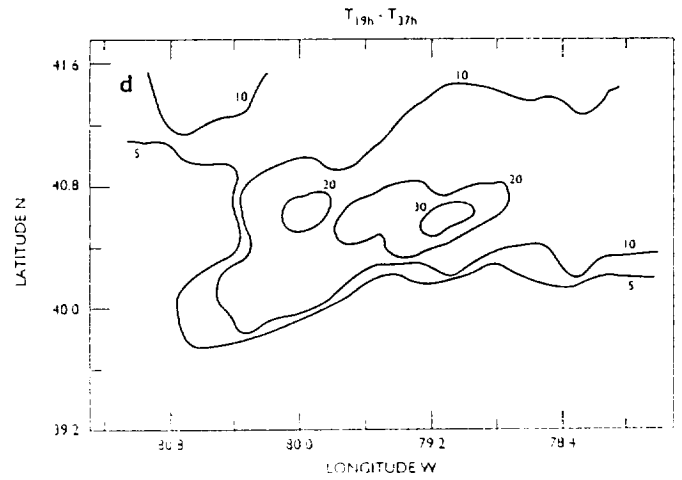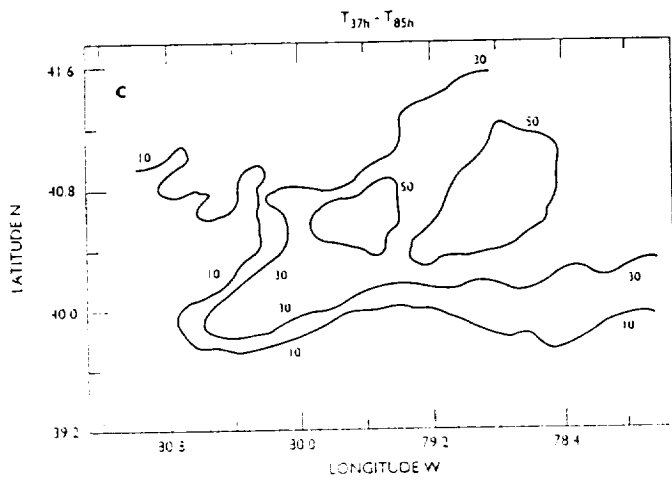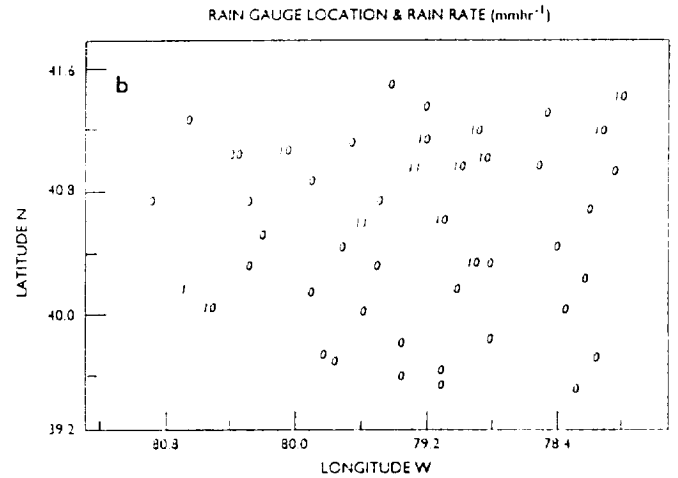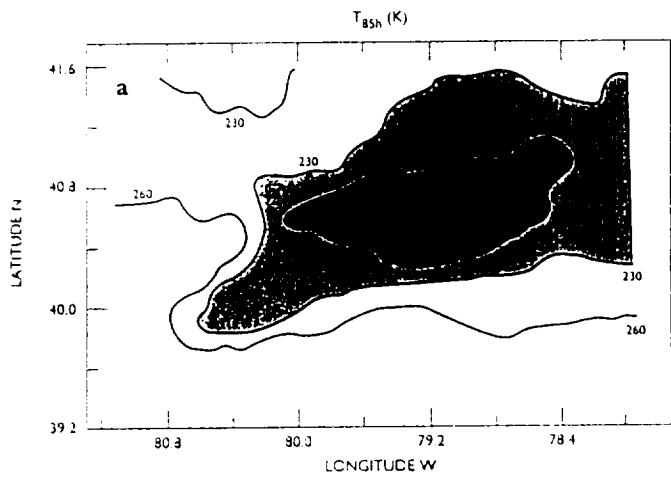
Figure 2: Maps of a) SSM/I T_{85h}, b) rain rate from 15-minute rain gauge, c) SSM/I T_{37h}-T_{85h}, and d) SSM/I T_{19h}-T_{37h} over a $2° \times 3°$ grid box in the Northeastern United States on 22 August '87 at 1119 UTC (619 EST). In **2a**, the prominent regions of strong scattering depression, i.e. $T_{85h} < 200$ K, are denoted by heavy shading. The regions where T_{85h} is between 200 K and 230 K are lightly shaded.

On land, when the surface gets wet, its emissivity decreases and hence the 37 GHz brightness temperature (T_{37h}) is diminished as compared to that on dry land (Prabhakara et al, 1995). This reduction in T_{37h} can be noticed because the radiation at this frequency is weakly absorbed by water vapor and oxygen in the atmosphere. In the 85 GHz channel of SSM/I, this absorption due to water vapor and oxygen in the atmosphere is relatively strong. For this reason, the effect of the surface wetness on T_{85h} is much less pronounced. In Figure 2c, we show a map of the difference signal, $T_{37h} - T_{85h}$. This difference is used to minimize impact of the surface wetness effect on T_{85h}. Essentially all of the salient features in Figure 2a are represented here. We may note that because of scattering, the brightness temperature in the 85 GHz channel is less than that of the 37 GHz. Thus, the difference signal, $T_{37h} - T_{85h}$, serves as a scattering index on land (see also Barrett et al., 1988), and is used in the subsequent rain analysis.

In order to show information about rain in the long wavelength channels at 19 and 37 GHz, we show in Figure 2d a map of the difference $T_{19h} - T_{37h}$ for this rain event. Examination of Figures 2a, c, and d reveal that there is substantial redundancy in the information of the 85, 37, and 19 GHz channels. However, information given by the high frequency channels (T_{37h} and T_{85h}) is preferred because of better sensitivity and spatial resolution.

Since the rain gauges have poor resolution, and are not dense in spatial coverage, we cannot show a scatter plot of rain rate versus T_{85h} for one event, as was done in Figure 1c. For this reason, we have taken the 15-minute rain gauge data over a large area of the Eastern United States (25-45 N and 75-84 W) for the month of Aug. '87 and compared it with the SSM/I T_{85h} measurements. We may note that these gauge and radiometer data are matched in space and time to within 4 km and

15 minutes, respectively. In Figure 3a, we show a scatter plot of these data. A similar figure for the Midwest United States (25-45 N and 88-97 W) is presented in Figure 3b. We notice from these plots that the rain rate is not related to T_{85h} in a simple fashion, which was found to be the case in Figure 1c over ocean. In Figure 3a, a prominent maximum near 230 K is apparent; while in Figure 3b, the "warm" and "cold" convective rain maxima are clearly seen. From these analyses shown Figures 1a-e, 2a-d, and 3a-b, one can see that the signal due to rain in the microwave radiometer data on land and ocean is broadly similar.

We may remark that the SSM/I data in the 19, 37, and 85 GHz channels are measured in dual polarization. We have examined the polarization information in all these channels, together with the rain observations over land and ocean. We find addition of this polarization information does not necessarily help us to improve quantitative estimation of rain rate.

From the above discussion, we find that the information contained in the multi-spectral, dual-polarization measurements of SSM/I is highly redundant. When there is rain, other hydrometeors - cloud liquid water and frozen and melting ice particles of different sizes, shapes, and densities - can also be present in a vertical column of the atmosphere. The radiometric contamination introduced by these other hydrometeors is not necessarily insignificant. Thus, with the limited information from the microwave radiometer, theoretical rain retrievals (see for eg. Wu and Weinman, 1984; Kummerow et al., 1989 and Smith and Mugnai, 1992) encounter insurmountable problems. We may note that this is not solely because of beam-filling and surface emissivity problems.
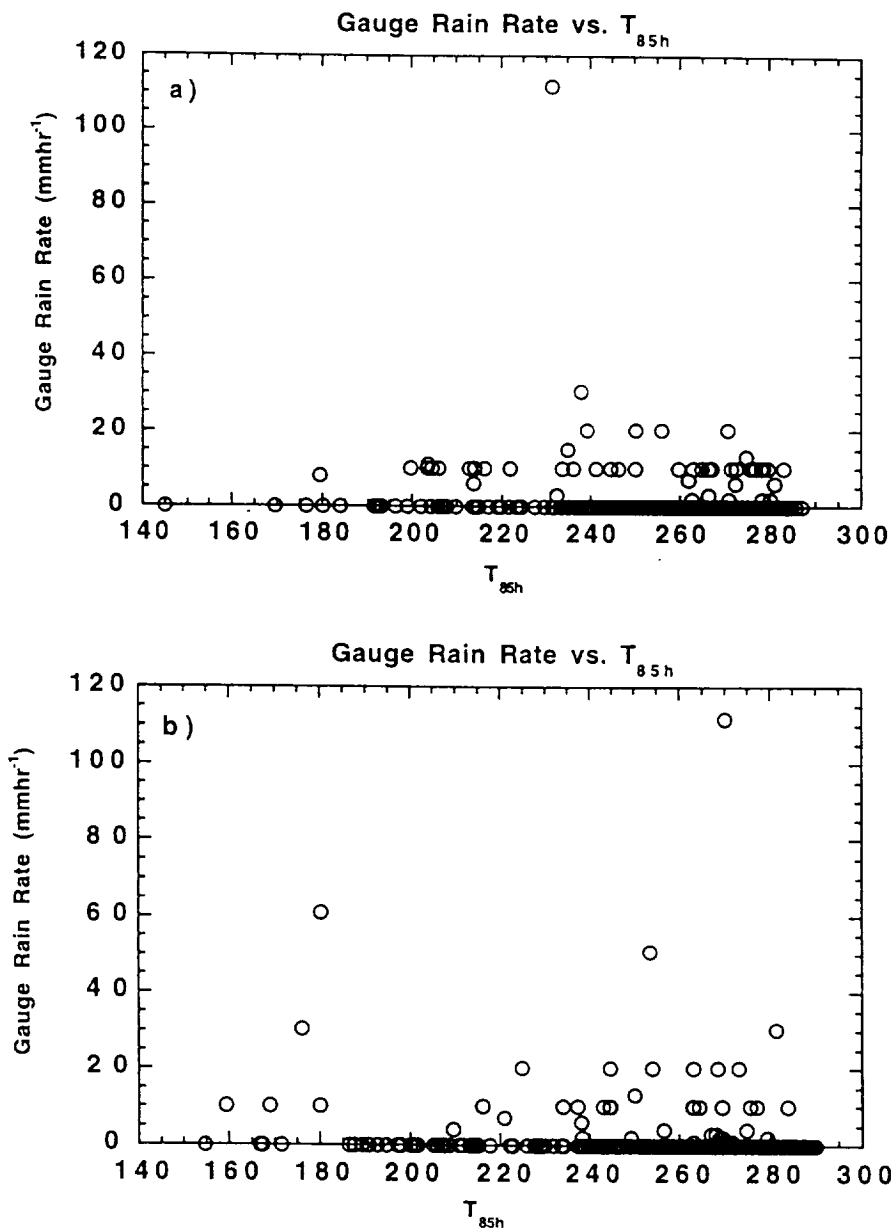
Figure 3: Scatter plot of coincident SSM/I T85h vs. rain gauge observations (mmhr⁻¹) over land in a) the Eastern United States (25-45 N and 75-84 W) and b) the Midwest United States (25-45 N and 88-97 W).

Because of these problems, in this study we have taken the path of mesoscale-average rain rate estimation using the microwave radiometer data. The basis for this approach is that a threshold on the 85 GHz scattering depression can be used to detect the presence of rain. This allows us to determine the rain area in a mesoscale region that exceeds this threshold. Then, this rain area can be related to mesoscale-average rain rate. By doing so, we ignore the details of the nature of rain on a small scale; but we attempt to capture the intensity of rain on a macroscopic scale.

3. Area-average rain retrieval method applicable to land

In this study, we derive the fractional rain area for three individual grid boxes of $2° \times 3°$ over a section of the Northeastern United States (39.5-41.5 N and 81-75 W) with the aid of $T_{37h} - T_{85h}$, which is denoted as δT_{37-85}. These three grid boxes exclude the area of the Great Lakes. The fractional rain area in a mesoscale grid box of $2° \times 3°$ is indicated with the symbol f_R, where f_R is given by

$$f_R = \frac{n}{N}. \tag{1}$$

In this equation, n is the number of 85 GHz rain footprints in a $2° \times 3°$ grid box, and N is the total number of 85 GHz footprints in that grid box. We have used values of 1, 2, 3, 4, and 8 K for δT_{37-85} as thresholds to detect the presence of rain. Of these thresholds, the best linear correlation between f_R and average rain rate is found when δT_{37-85} is 3 K. The 3 K threshold on δT_{37-85} is used throughout the remainder of this study to determine f_R.

We have compiled nine months of SSM/I measurements (Mar. '88 - Nov. '88) in the three grid boxes. In this compilation, only those passes that have grid boxes that are fully covered by the satellite data are retained. From these data, we have deduced f_R for each grid box and the corresponding mean of δT_{37-85} over

the rain area f_R , i.e., $(\overline{\delta T_{37-85}})$. In a given grid box for each satellite pass, the ground-truth, grid-box-average rain rate is obtained by averaging the 15-minute rain gauge data. In order to ensure a robust estimate of this average, we require that there should be at least 40 gauges in a given grid box. This average rain rate is denoted by $R_{\geq 40}$. This $R_{\geq 40}$ is compared with f_R and $\overline{\delta T_{37-85}}$ with the data presented in Table 1 for one grid box (39.5-41.5 N and 78-81 W) for the full nine months.

In Figure 4a, a scatter plot of $R_{\geq 40}$ versus f_R is presented for the nine months of data given in Table 1. The correlation coefficient between these variables is shown in the figure. Similarly, in Figure 4b, a scatter plot of $R_{\geq 40}$ versus $\overline{\delta T_{37-85}}$ and the correlation coefficient between these two variables is presented. From these figures, we note that f_R explains a significantly larger fraction of the variance in $R_{\geq 40}$ than $\overline{\delta T_{37-85}}$.

We have computed grid-box-mean, i.e. mesoscale-average, rain rate using a retrieval formula that is similar to that presented in Prabhakara et al. (1998). The form of that equation is given below:

$$R_X = \exp\left[\psi_X X\right] - 1. \tag{2}$$

The retrieved rain rate R_X given by the above equation depends on the argument X and the scaling constant ψ_X shown in the exponent. Substituting the argument X with f_R and $\overline{\delta T_{37-85}}$, we have estimated mesoscale-average rain rates R_{f_R} and R_{37-85}, respectively. In Figures 5a and 5b, $R_{\geq 40}$ is compared against R_{f_R} and R_{37-85}, respectively. We find that R_{f_R} explains 66 % of the variance contained in $R_{\geq 40}$, while R_{37-85} explains only 21 %. Although we have not presented for this case

11

Grid-Box-Average Gauge Rain Rate vs Fractional Rain Area

a)

Corr. Coeff. = 0.81

Grid-Box Average Gauge Rain Rate (mmhr^{-1})

Fractional Rain Area

Grid-Box-Average Gauge Rain Rate vs. Scattering Depression $(T_{37h} - T_{85h})_{ave}$

b)

Corr. Coeff. = 0.46

Grid-Box-Average Gauge Rain Rate (mmhr^{-1})

$(T_{37h} - T_{85h})_{ave}$ (K)

Figure 4: a) Relationship between the fractional rain area f_R and the corresponding grid-box-average rain rate $R_{\geq 40}$ deduced from 15-minute rain gauge observations. b) Relationship between the scattering index $(T37h-T85h)$ and the corresponding grid-box-average rain rate $R_{\geq 40}$ deduced from 15-minute rain gauge observations.
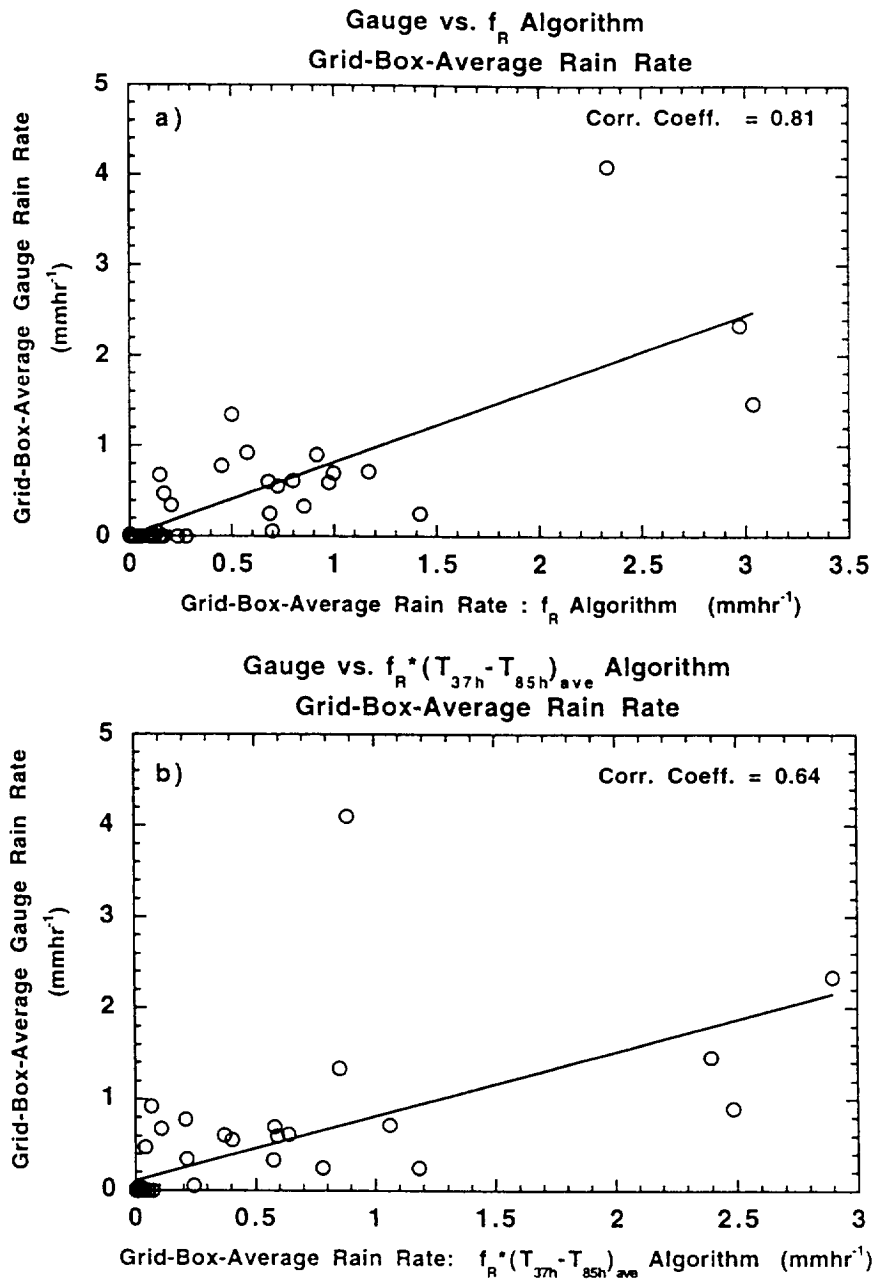
Figure 5: Scatter plot of $R_{\geq 40}$ versus grid-box-average rain rate retrieved using the equations a) $R_{f_R} = \exp[0.036 \bullet f_R] - 1$ and b) $R_{37-85} = \exp[0.003 \bullet f_R \bullet \overline{\delta T_{37-85}}] - 1$. These plots represent data for nine months of 1988 (Mar. '88 - Nov. '88) in a grid box (39.5-41.5 N and 78-81 W) in the Northeastern United States.

results from substituting X with simple linear and non-linear combinations of the two basic variables f_R and $\overline{\delta T_{37-85}}$, we find that the retrieved rain rates from such combinations explain significantly less than 66 % of the variance contained in $R_{\geq 40}$.

The NASA/GSCAT and NOAA/SRL rain retrieval algorithms, applicable to the radiometer footprint scale, are presented in detail by Conner and Petty (1998). These algorithms have built in thresholds on the 85 GHz brightness temperature, as well as some screening procedures to eliminate questionable surface emissivity conditions. We have implemented these algorithms in this study and computed rain rates on a pixel scale for each satellite pass in each grid box. In order to compare these results with $R_{\geq 40}$, we have averaged these pixel-scale rain rate estimates in each grid box for each satellite pass. These grid-box average rain rates for the NASA/GSCAT and NOAA/SRL rain retrieval algorithms are denoted as R_{GSCAT} and R_{SRL}, respectively. We may remark that since both R_{GSCAT} and R_{SRL} are based on thresholds on the 85 GHz brightness temperature, these grid-box average rain rates reflect the joint effect of the rain area in the grid box as well as the 85 GHz scattering index. In Figures 6a and 6b, we have compared these rain rates with $R_{\geq 40}$. The NASA/GSCAT and NOAA/SRL rain retrieval algorithms can explain respectively about 18 % and 14 % of the variance contained in nine months of the ground-truth rain rate data over this grid box in the Northeastern United States.

We have retrieved grid-box-average rain rates for the other two grid boxes over the Northeastern United States for the same nine-month time period. These are the only two other $2^{o} \times 3^{o}$ grid boxes in the United States where the number of 15-minute rain gauges exceeds 40 in each grid box. In Table 2 combining the data for all three grid boxes, we compare the relative merits of the rain rate retrieved from Equation 2 when X is substituted by f_R and the product $f_R \cdot \overline{\delta T_{37-85}}$. The rain rates
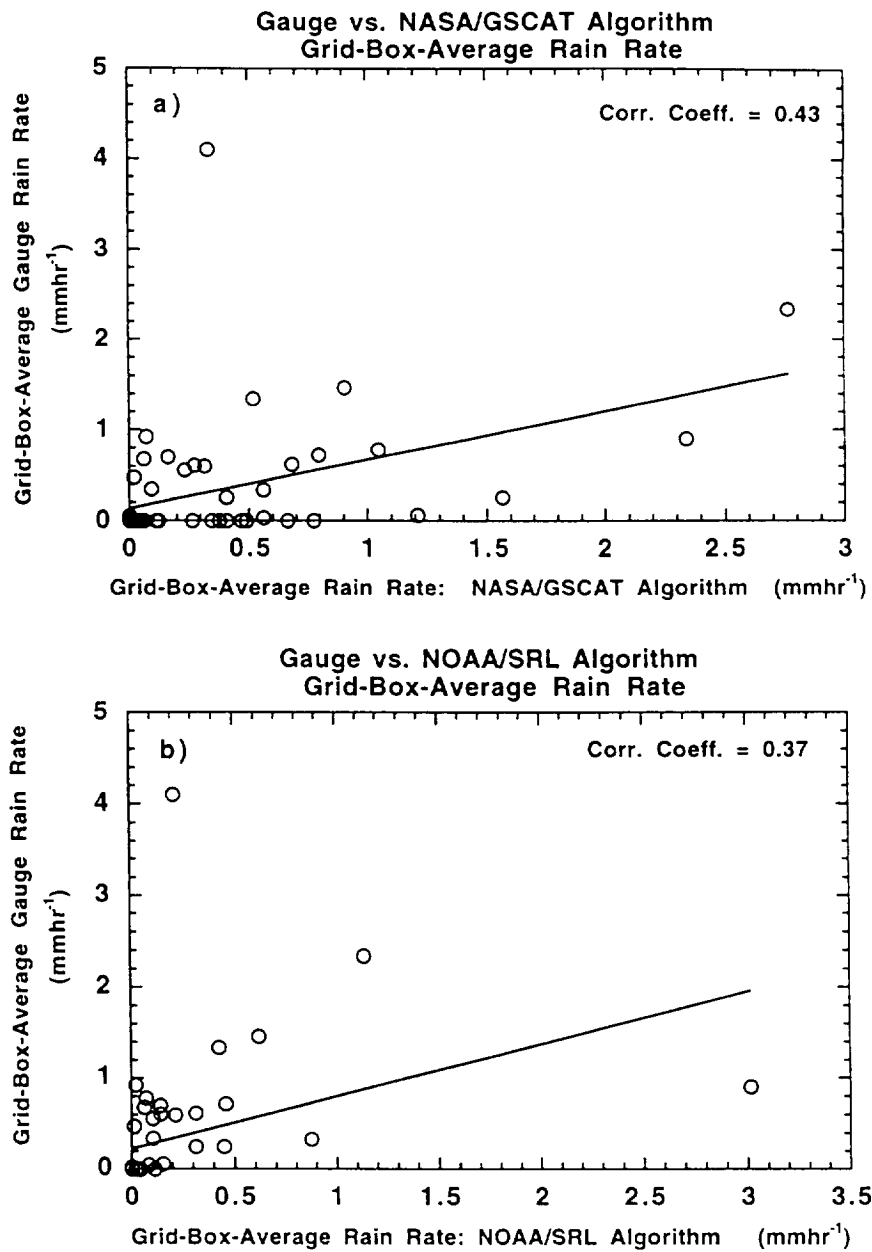
Figure 6: Scatter plot of $R_{\geq 40}$ versus mesoscale-average rain rate retrieved using a) NASA/GSCAT and b) NOAA/SRL algorithms. These plots represent data for nine months of 1988 (Mar. '88 - Nov. '88) in a grid box (39.5-41.5 N and 78-81 W) in the Northeastern United States.

retrieved from the NASA/GSCAT and NOAA/SRL algorithms are also included in this table for comparison. From this comparison, we conclude that the grid-box-average rain rate retrieved from f_R, shown in the first row of the table, can explain about 64 % of the variance contained in the ground-truth rain observations in all three grid boxes. Performance of this algorithm is better than that of the others, except in one grid box.

The reason why the algorithm based on f_R performs better than the NASA/GSCAT and NOAA/SRL algorithms is explained as follows. In the fractional rain area algorithm, only f_R gives the grid-box-average rain rate. On the other hand, in the other algorithms both the rain area and the scattering information enter into the retrievals. As long as f_R and the scattering information are correlated, we expect good retrievals. On the contrary, when this correlation is poor, the retrievals are degraded. The correlation between f_R and the scattering information in a given period and grid box deteriorates when there are some events in that period where f_R is relatively large and the scattering information is weak. The poor results shown in rows 3 and 4 of Table 2 for grid boxes 2 and 3, representing the performance of the rain retrievals of NASA/GSCAT and NOAA/SRL, can be explained with the above reasoning.

When the data from all three grid boxes are put together, we find that R_{f_R} can explain 50 % more of the variance contained in $R_{\geq 40}$, as compared to R_{GSCAT} and R_{SRL}. All three algorithms have inherent in them the concept of the rain area. To a first-order approximation, one may expect that the average rain rate in a grid box increases as the rain area increases. However, because the NASA/GSCAT and NOAA/SRL algorithms use additionally the information of the 85 GHz scattering index, these rain retrievals deteriorate. This result can be inferred from the non-

13

monotonic relationship between the ground-truth rain rate and T_{85h} shown in Figures 1c, 3a and 3b on a footprint scale. Because of this reason, even when the ground-truth rain rate and T_{85h} are averaged over a mesoscale area, they relate only poorly with one another.

4. Procedure to retrieve rainfall on land in the TRMM mission

The method described earlier gives a radar-quality, monthly-mean rain rate in a mesoscale grid box. A brief summary of the procedure to apply this rain retrieval method to TRMM radiometer and radar data is presented in the following:

1) From the 760 km wide swath of TRMM Microwave Imager (TMI) radiometer data, extract a 220 km swath of data centered on the satellite orbital track. This data overlaps exactly with the TRMM radar observations. Bin these TMI data into a fixed geographic grid of $2^\circ \times 3^\circ$. For each pass of the TRMM satellite over a given grid box, the collocated TMI and radar data will generally fill a variable portion of that grid box. This variable portion of a grid box is considered to be a mesoscale area. For purpose of TRMM, we will accept for the rain retrievals only those events that fill at least 50 % of a given grid box with collocated TMI and Precipitation Radar data.

2) Within a given month, for each grid box in the land regions from 35 S to 35 N covered by the TRMM satellite, do the following:

    a) Determine the number of rain events. Then, utilizing the TMI data, estimate the fractional rain area, f_R, for each of these rain events. Also, from the radar data, determine the average rain rate R_A for each rain event.

14

b) Given f_R and R_A, determine ψ_{f_R} using Eq. 2 such that the sum of R_{f_R} from the radiometer and the sum of R_A from radar for all the rain events in the month are equal,

i.e.,
$$\sum_{i=1}^{N_m} \left(R_{f_R} \right)_i = \sum_{i=1}^{N_m} (R_A)_i .$$

In the above summation, N_m stands for the total number of rain events in that month. The above condition also means that the monthly-mean values $\overline{R}_{f_R}$ and $\overline{R}_A$ are equal.

Procedures 1 and 2 will create a map of ψ_{f_R} with a resolution of $2^\circ \times 3^\circ$ over the land areas from 35°N to 35°S for a given month. Then, using all of the 760 km wide swath of TMI radiometer data, we can derive area-average rain rates in each $2^\circ \times 3^\circ$ grid box for each rain event detected by the TMI. In this manner, in a month each grid box is sampled by the TMI about 3.5 times more often than by the radar. From these gridded data, the $5^\circ \times 5^\circ$ monthly-mean rainfall as required by the TRMM mission (Simpson et al., 1996) can be determined by suitable averaging.

5. Discussion and conclusions

In this study, we indicate that on a footprint scale the limited amount of information contained in the multi-channel, dual-polarization SSM/I microwave radiometer measurements over land and ocean is not sufficient to resolve different types of hydrometeors or rain intensity in a satisfactory fashion. This is primarily because the information conveyed by these channels is highly redundant and is not capable of discriminating different kinds of hydrometeors and their vertical profiles.

15

The radiometer data on the other hand can identify reasonably well the presence of rain for rain rates above a relatively small threshold. This allows us to determine the rain area in a mesoscale region that exceeds this threshold. We find that as this rain area increases the mesoscale-average rain rate increases. This result is simple and is consistent with the findings of earlier investigators (Doneaud et al., 1984, and Lopez et al., 1989). Area-average rain rate in three $2^{o} \times 3^{o}$ grid boxes over the Northeastern United States (39.5-43.5 N and 75-81 W) estimated with this retrieval method for nine months has a correlation of 0.79 with rain rate derived from 15-minute rain gauges. We find that adding the spectral information from the radiometer to the retrieval algorithm causes the results to deteriorate. This result is borne out by the NASA/GSCAT and NOAA/SRL algorithms, where inherently the rain area and spectral information are combined. This result can be inferred from the non-monotonic relationship between the ground-truth rain rate and T_{85h} shown in Figures 1c, 3a and 3b.

A similar analysis (Prabhakara et al., 1998) presented for the TOGA-COARE region showed that the spectral information helped only marginally in explaining the variance of the ground-truth radar rain rates. However, on the land, probably because of more vigorous convective activity, we find that the spectral information degrades the rain retrievals.

We find that the area-average rain retrieval method requires ground truth that has good sensitivity and areal coverage. This requirement will be met when the TRMM radar rain rate observations are available. Additionally, the field of the view of the TRMM radiometer is about one third that of the SSM/I, which should enable us to define the fractional rain area much more accurately. We believe that

16

these benefits should give improved results when the algorithm is applied to the TRMM data.

In the TRMM mission, the radar observations are limited to a narrow swath of 220 km, while the microwave radiometer observations extend over a swath of 760 km. Using the coincident TRMM radiometer and radar data, we can calibrate our area-average rain rate retrieval method. With this calibrated method, we can extend the temporal and spacial coverage of the radar observations, and thus get an improved rainfall climatology.

References

Adler, R. F., G. J. Huffman, and P. R. Keehn, 1994: Global tropical rain estimates from microwave-adjusted geosynchronous IR data. *Remote Sens. Rev.,* **11** 125-152.

Barrett, E. C., C. Kidd, and J. O. Bailey, 1988: Special Sensor Microwave Imager: A new instrument with rainfall measuring potential. *Int. J. Remote Sens.,* **9**, 1943-1950.

Battan, L. J., 1973: *Radar Observations of the Atmosphere.* The University of Chicago Press, 324 pp.

Conner, M. D., and G. W. Petty, 1998: Validation and intercomparison of SSM/I rain-rate retrieval methods over the continental United States. *J. Appl. Met.,* **37**, 679-700.

Doneaud, A. A., S. Ionescu-Niscov, D. L. Priegnitz, and P. L. Smith, 1984: The Area Time Integral as an indicator for convective rain volume. *J. Clim. Appl. Met,* **23** , 555-561.

Ebert, E. E., M. J. Manton, P. A. Arkin, R. J. Allam, G. E. Holpin, and A. Gruber, 1996: Results from the GPCP Algorithm Intercomparison Programme. *Bull. of Am. Met Soc.*, **77**, 2875-2887.

Ferraro, R. R., and G. F. Marks, 1995: The development of SSM/I rain-rate retrieval algorithms using ground-based radar measurements. *J. Atmos. Oceanic Technol.*, **12**, 755-770.

Grody, N. C., 1991: Classification of snow cover and precipitation using the Special Sensor Microwave/Imager. *J. Geophys. Res.*, **96**, 7423-7435.

Heymsfield, G. M., I. J. Caylor, J. M. Shepherd, W. S. Olson, S. W. Bidwell, W. C. Boncyk, and S. Ameen. 1996: Structure of Florida thunderstorms using high altitude aircraft radiometer and radar observations. *J. Appl. Met,* **35**, 1736-1762.

Hollinger, J., R. C. Lo, G. Poe, R. Savage, and J. Pierce, 1987: *Special Sensor Microwave Imager Guide.* Naval Research Laboratory, Washington, D.C., 120 pp.

Houze Jr., R. A., 1997: Stratiform precipitation in regions of convection: A meteorological paradox? *Bull. Amer. Met. Soc.,* **78**, 2179-2196.

Kummerow, C., R. A. Mack, and I. M. Hakkarinen, 1989: A self-consistency approach to improved microwave rainfall estimation from space. *J. Appl. Met,* **28**, 869-884.

Lopez, R. E., D. Atlas, D. Rosenfeld, J. L. Thomas, D. O. Blanchard, and R. L. Holle, 1989: Estimation of rainfall using the Radar Echo Area Time Integral. *J. Appl. Met,* **28**, 1162-1175.

McGhaughey, G. and E. Zipser, 1996: Passive microwave observations of the stratiform regions of two tropical oceanic Mesoscale Convective Systems. *J. Appl. Met,* **35**, 1949-1962.

18

Meneghini, R. 1996: *Analysis of radar and radiometer methods for space borne measurements of precipitation.* Ph.D. Thesis. Kyoto University.

Oki, R., A. Sumi, and D. A. Short, 1997: Sampling simulation of TRMM rainfall estimation using Radar-AMeDAS composites. *J. Appl. Met,* **36**, 1480-1492.

Olson, W. S., C. Kummerow, G. M. Heymsfield, and L. Giglio, 1996: A method for combined passive-active microwave retrievals of cloud and precipitation profiles. *J. Appl. Met,* **35**, 1763-1789.

Prabhakara, C., G. Dalu, G. L. Liberti, J. J. Nucciarone, and R. Suhasini, 1992: Rainfall over oceans : Remote sensing from satellite microwave radiometers. *Met and Atmos. Phys.,* **47**, 177-199.

Prabhakara, C,. J.J. Nucciarone, and Jung-Moon Yoo, 1995: Examination of ' Global Atmospheric Temperature Monitoring with Satellite Microwave Measurements': 1) Theoretical Considerations, *Climatic Change ,* **30**, 349-366.

Prabhakara, C., R. Iacovazzi, Jr., R. Meneghini, R. Oki, D. A. Short, M. Cadeddu, and J. A. Weinman, 1998: A TRMM microwave radiometer rain retrieval technique based on fractional rain area, *J. of Met. Soc. of Japan ,* **76**, 765-781.

Schols, J. L., J. A. Weinman, R. E. Stewart, and R. P. Lawson, 1995: The retrieval of dry and wet snow distributions from SSM/I measurements and MM5 forecast results. *Proceedings of International Geosciences and Remote Sensing Symposium.* IGARSS'95.

Simpson, J., C. Kummerow, W.-K. Tao, and R. F. Adler, 1996: On the tropical rainfall measuring mission (TRMM). *Met and Atmos. Phys.,* **60**, 19-36.

Short, D. A., P. A. Kucera, B. S. Ferrier, J. C. Gerlach, S. A. Rutledge, and O. W. Thiele, 1997: Shipboard radar rainfall patterns within the TOGA/COARE IFA. *Bull. of Am. Met Soc.,* **78**, 2817-2836.

Smith, E. A. and A. Mugnai, 1992: Foundations for statistical-physical precipitation retrieval from passive microwave satellite measurements. Part 1: Brightness temperature properties of a time-dependent cloud radiation model. *J. Appl. Met*, **31**, 532-552.

Wu, R. and J. A. Weinman, 1984: Microwave radiances from precipitating clouds containing aspherical ice, combined phase, and liquid hydrometeors. *J. Geophy. Res.*, **89**, 7170-7178.

Figure Captions

Figure 1: Maps of **a)** SSM/I T_{85h} and **b)** the coincident radar rain rate data in the TOGA-COARE region for 24 Dec. '92 at 1031 UTC. In **1b**, regions with intense rain rate (> 4 mmhr^{-1}) are identified with light shading and cross hatching. This differentiation is done on the basis of the information given in the map of T_{85h} presented in **1a**. Light-shaded areas correspond to regions where T_{85h} is relatively warm (~ 260 K); while the cross-hatched areas correspond to regions where T_{85h} is cold (< 200 K). **c)** Scatter plot of coincident 85 GHz SSM/I radiometer brightness temperature (K) measurements and radar rain observations (mmhr^{-1}) over the TOGA-COARE region. **d)** Map of SSM/I T_{37h} in the TOGA-COARE region for 24 Dec. '92 at 1031 UTC. **e)** Scatter plot of coincident 37 GHz SSM/I radiometer brightness temperature (K) measurements and radar rain observations (mmhr^{-1}) over the TOGA-COARE region.

Figure 2: Maps of **a)** SSM/I T_{85h}, **b)** rain rate from 15-minute rain gauge, **c)** SSM/I T_{37h}-T_{85h}, and **d)** SSM/I T_{19h}-T_{37h} over a $2^{o} \times 3^{o}$ grid box in the Northeastern United States on 22 August '87 at 1119 UTC (619 EST). In **2a**, the prominent regions of strong scattering depression, i.e. $T_{85h} < 200$ K, are denoted by heavy shading. The regions where T_{85h} is between 200 K and 230 K are lightly shaded.

Figure 3: Scatter plot of coincident SSM/I T_{85h} vs. rain gauge observations (mmhr^{-1}) over land in **a)** the Eastern United States (25-45 N and 75-84 W) and **b)** the Midwest United States (25-45 N and 88-97 W).

Figure 4: **a)** Relationship between the fractional rain area f_R and the corresponding grid-box-average rain rate $R_{\geq 40}$ deduced from 15-minute rain gauge observations. **b)** Relationship between the scattering index $(T_{37h}\text{-}T_{85h})$ and the corresponding grid-box-average rain rate $R_{\geq 40}$ deduced from 15-minute rain gauge observations.

Figure 5: Scatter plot of $R_{\geq 40}$ versus grid-box-average rain rate retrieved using the equations **a)** $R_{f_R} = \exp[0.036 \bullet f_R] - 1$ and **b)** $R_{37\text{-}85} = \exp[0.003 \bullet f_R \bullet \overline{\delta T_{37-85}}] - 1$. These plots represent data for nine months of 1988 (Mar. '88 - Nov. '88) in a grid box (39.5-41.5 N and 78-81 W) in the Northeastern United States.

Figure 6: Scatter plot of $R_{\geq 40}$ versus mesoscale-average rain rate retrieved using **a)** NASA/GSCAT and **b)** NOAA/SRL algorithms. These plots represent data for nine months of 1988 (Mar. '88 - Nov. '88) in a grid box (39.5-41.5 N and 78-81 W) in the Northeastern United States.

Table 1. The data in a $2^\circ \times 3^\circ$ grid box within the Northeastern United States (39.5-41.5 N and 78-81 W) for the nine month period Mar. '88 to Nov. '88 used for area-average rain retrieval. The data is as follows:

Jday/Mon - Julian day and month

Pass - Satellite pass relative to 0000 UTC of the 1st day of a given month

n - Number of 85 GHz rain pixels

N - Total number of 85 GHz pixels

fR - n/N Fractional rain area

T37-85av - δT_{37-85} averaged over fR, i.e., $\overline{\delta T_{37-85}}$

#G - Number of rain gauges

RG - Area-average rain rate deduced from 15-minute rain gauges, i.e., $R_{\geq 40}$

R1 - Area-average rain rate retrieved using $R_{f_R} = \exp[0.036 \cdot f_R] - 1$

R2 - Area-average rain rate retrieved using $R_{37\text{-}85} = \exp\left[0.003 \cdot f_R \cdot \overline{\delta T_{37-85}}\right] - 1$

R3 - Area-average rain rate retrieved using NASA/GSCAT algorithm

R4 - Area-average rain rate retrieved using NOAA/SRL algorithm

Jday	/Mon	Pass	n	N	fR	T37-85av	#G	RG	R1	R2	R3	R4
85	Mar'88	49	0	352	0.000	0.0	41	0.000	0.000	0.000	0.000	0.000
92	Apr'88	2	11	458	0.026	1.9	43	0.000	0.096	0.015	0.000	0.041
92		1	5	368	0.014	1.7	45	0.000	0.050	0.007	0.020	0.020
99		14	0	355	0.000	0.0	43	0.020	0.000	0.000	0.000	0.000
126	May'88	9	78	337	0.231	8.1	43	0.335	0.850	0.573	0.559	0.874
131		18	90	366	0.249	32.4	46	0.904	0.913	2.485	2.337	3.018
140		36	112	353	0.317	10.9	45	0.721	1.167	1.060	0.792	0.457
140		37	15	329	0.046	3.0	43	0.478	0.167	0.042	0.020	0.010
140		38	66	358	0.184	6.6	43	0.610	0.677	0.372	0.274	0.142
153	Jun'88	1	7	465	0.015	2.1	44	0.000	0.055	0.010	0.000	0.000
183	Jul'88	1	0	355	0.000	0.0	54	0.000	0.000	0.000	0.030	0.000
201		37	99	369	0.271	7.0	45	0.701	0.996	0.580	0.163	0.142
202		39	80	435	0.186	13.7	40	0.254	0.683	0.781	0.406	0.315
204		42	0	420	0.000	0.0	48	0.000	0.000	0.000	0.000	0.000
214	Aug'88	1	0	386	0.000	0.0	50	0.000	0.000	0.000	0.000	0.000
214		2	0	371	0.000	0.0	49	0.000	0.000	0.000	0.000	0.000
232		37	12	361	0.036	1.0	44	0.051	0.132	0.011	0.000	0.081
232		38	0	398	0.000	0.0	44	0.000	0.000	0.000	0.000	0.000
237		46	56	410	0.137	20.4	47	1.341	0.501	0.853	0.518	0.427

242		57	239	381	0.630	4.6	46	4.105	2.330	0.887	0.335	0.213
246	Sep'88	2	0	368	0.000	0.0	104	0.000	0.000	0.000	0.000	0.000
247		5	0	443	0.000	0.0	72	0.000	0.000	0.000	0.000	0.000
248		7	309	378	0.817	9.5	90	1.463	3.035	2.395	0.904	0.620
248		8	17	451	0.040	8.8	90	0.681	0.146	0.107	0.061	0.061
256		24	112	423	0.265	7.3	68	0.599	0.973	0.591	0.315	0.213
262		34	0	379	0.000	0.0	86	0.000	0.000	0.000	0.000	0.000
264		40	0	381	0.000	0.0	74	0.000	0.000	0.000	0.000	0.030
264		39	22	396	0.056	12.6	76	0.345	0.204	0.214	0.091	0.102
268		47	18	422	0.045	0.4	44	0.000	0.165	0.005	0.041	0.000
269		48	54	352	0.156	1.4	44	0.925	0.573	0.067	0.071	0.020
270		50	0	385	0.000	0.0	40	0.000	0.000	0.000	0.000	0.000
275	Oct'88	1	0	383	0.000	0.0	104	0.000	0.000	0.000	0.000	0.000
284		19	0	454	0.002	1.8	80	0.000	0.008	0.001	0.264	0.000
286		22	25	403	0.064	3.6	42	0.000	0.236	0.071	0.772	0.020
294		38	0	419	0.000	0.0	54	0.000	0.000	0.000	0.345	0.020
296		43	0	430	0.000	0.0	68	0.000	0.000	0.000	0.051	0.000
296		42	2	351	0.006	0.1	84	0.000	0.021	0.000	0.467	0.000
296		44	0	365	0.000	0.0	66	0.000	0.000	0.000	0.112	0.000
297		46	16	427	0.040	0.8	74	0.000	0.146	0.010	0.061	0.000
297		45	1	374	0.003	0.3	76	0.000	0.010	0.000	0.660	0.000
298		47	40	325	0.123	5.6	78	0.782	0.451	0.210	1.046	0.071
303		56	2	371	0.005	0.6	46	0.000	0.020	0.001	0.488	0.000
306	Nov'88	1	12	354	0.034	5.0	100	0.000	0.124	0.052	0.376	0.020
307		3	0	359	0.000	0.0	40	0.000	0.000	0.000	0.406	0.041
309		7	84	387	0.217	9.6	76	0.620	0.797	0.637	0.681	0.315
310		8	0	394	0.000	0.0	76	0.000	0.000	0.000	0.000	0.000
311		10	2	378	0.008	0.4	92	0.000	0.029	0.001	0.020	0.000
312		12	61	327	0.190	4.2	64	0.061	0.696	0.243	1.209	0.152
313		15	0	331	0.000	0.0	54	0.000	0.000	0.000	0.122	0.112
313		16	0	402	0.000	0.0	54	0.000	0.000	0.000	0.000	0.000
315		19	0	353	0.000	0.0	44	0.000	0.000	0.000	0.010	0.000
319		26	0	389	0.000	0.0	92	0.000	0.000	0.000	0.376	0.000
321		32	78	396	0.197	6.7	44	0.559	0.723	0.403	0.234	0.102
324		37	146	382	0.385	10.0	40	0.254	1.417	1.180	1.565	0.447
325		39	289	361	0.801	11.7	92	2.337	2.971	2.896	2.764	1.138
332		53	28	371	0.075	1.6	68	0.000	0.277	0.037	0.010	0.000
333		55	12	445	0.029	3.1	58	0.030	0.107	0.028	0.559	0.000

.

Table 2. Correlation coefficients between retrieved grid-box-average rain rate and gauge rain rate for three grid boxes in the Northeastern United States for nine months of 1988 (Mar. '88 - Nov. '88).

Rain Retrieval Method	Grid Box 1 (39.5-41.5 N, 78-81 W)	Grid Box 2 (39.5-41.5 N, 75-78 W)	Grid Box 3 (41.5-43.5 N, 75-78 W)
$R_{f_R} = \exp[0.036 \bullet f_R] - 1$	0.81	0.79	0.81
$R_{37\text{-}85} = \exp[0.003 \bullet f_R \bullet \overline{\delta T_{37-85}}] - 1$	0.64	0.85	0.73
NOAA/GSCAT	0.43	0.78	0.67
NOAA/SRL	0.37	0.89	0.67

T_{85h} (K)

a

LONGITUDE E

LATITUDE S

Fig. 1a

B1099.001

RADAR RAIN RATE (mmhr^{-1})

b

LATITUDE S

LONGITUDE E

Fig. 11.

B1099 002

Radar Rain Rate vs. T_{85h}

Fig. 1c

T_{37h} (K)

d

LONGITUDE E

LATITUDE S

Fig. 1d

B1099.003

Radar Rain Rate vs. T_{37h}

e)

Radar Rain Rate (mmhr^{-1})

T_{37h} (K)

Fig. 1e

T_{85h} (K)

a

LATITUDE N

LONGITUDE W

Fig. 2a
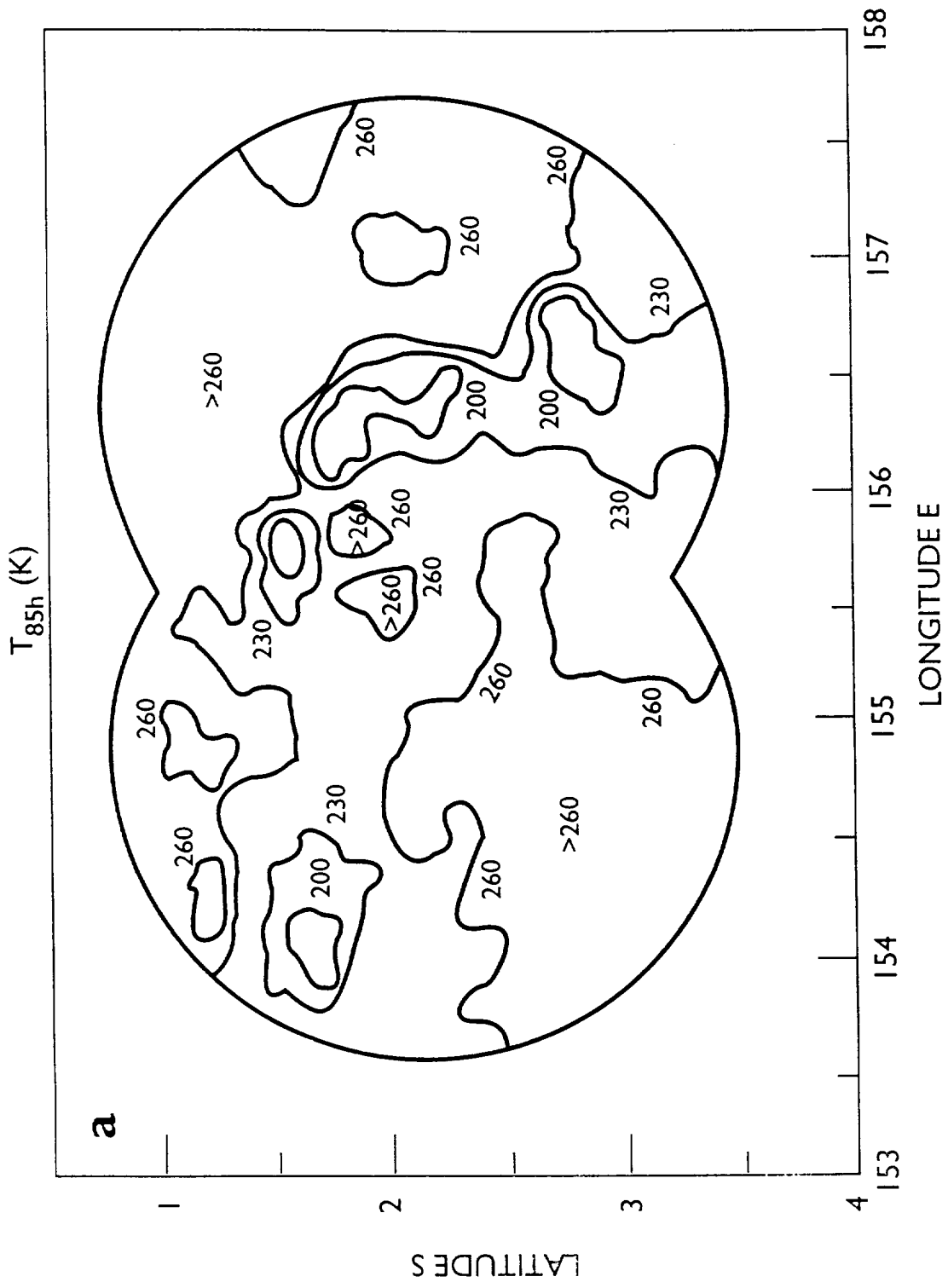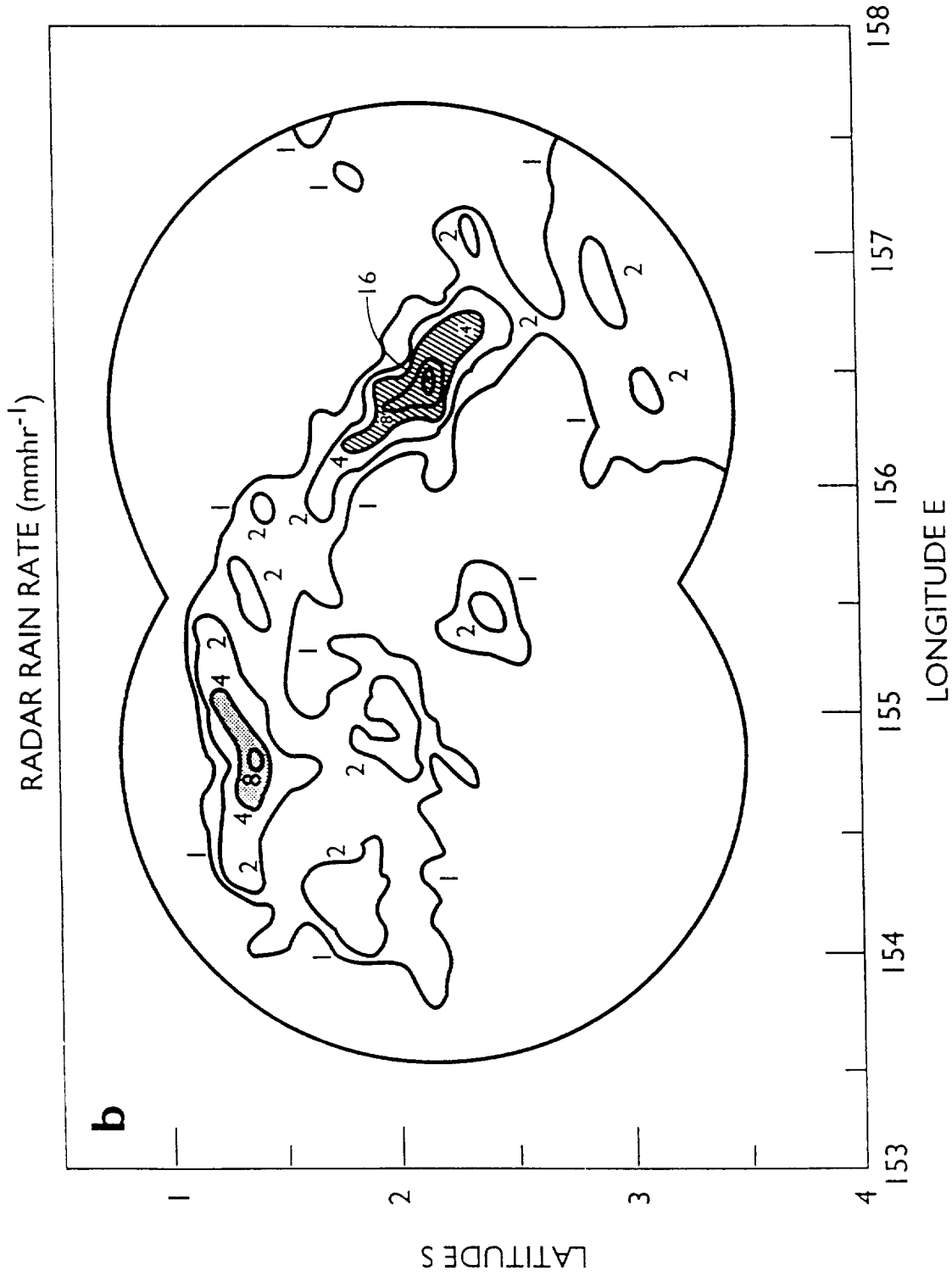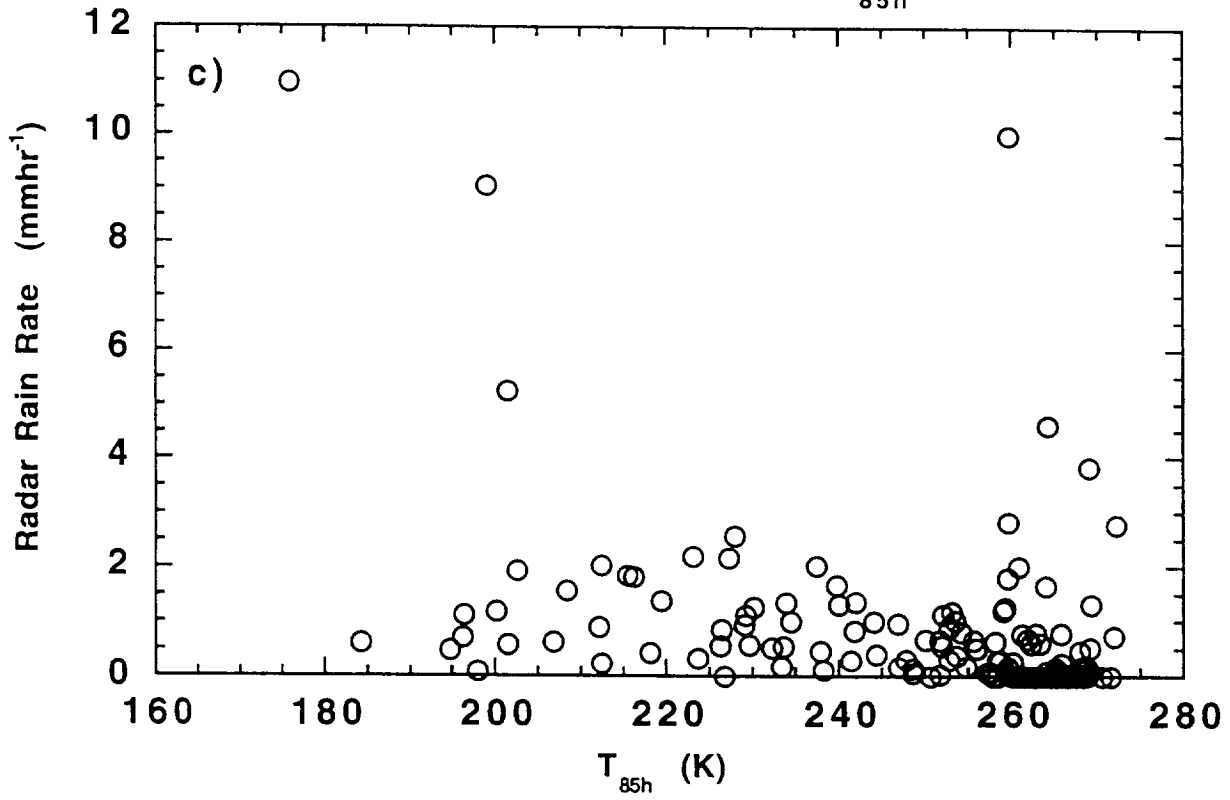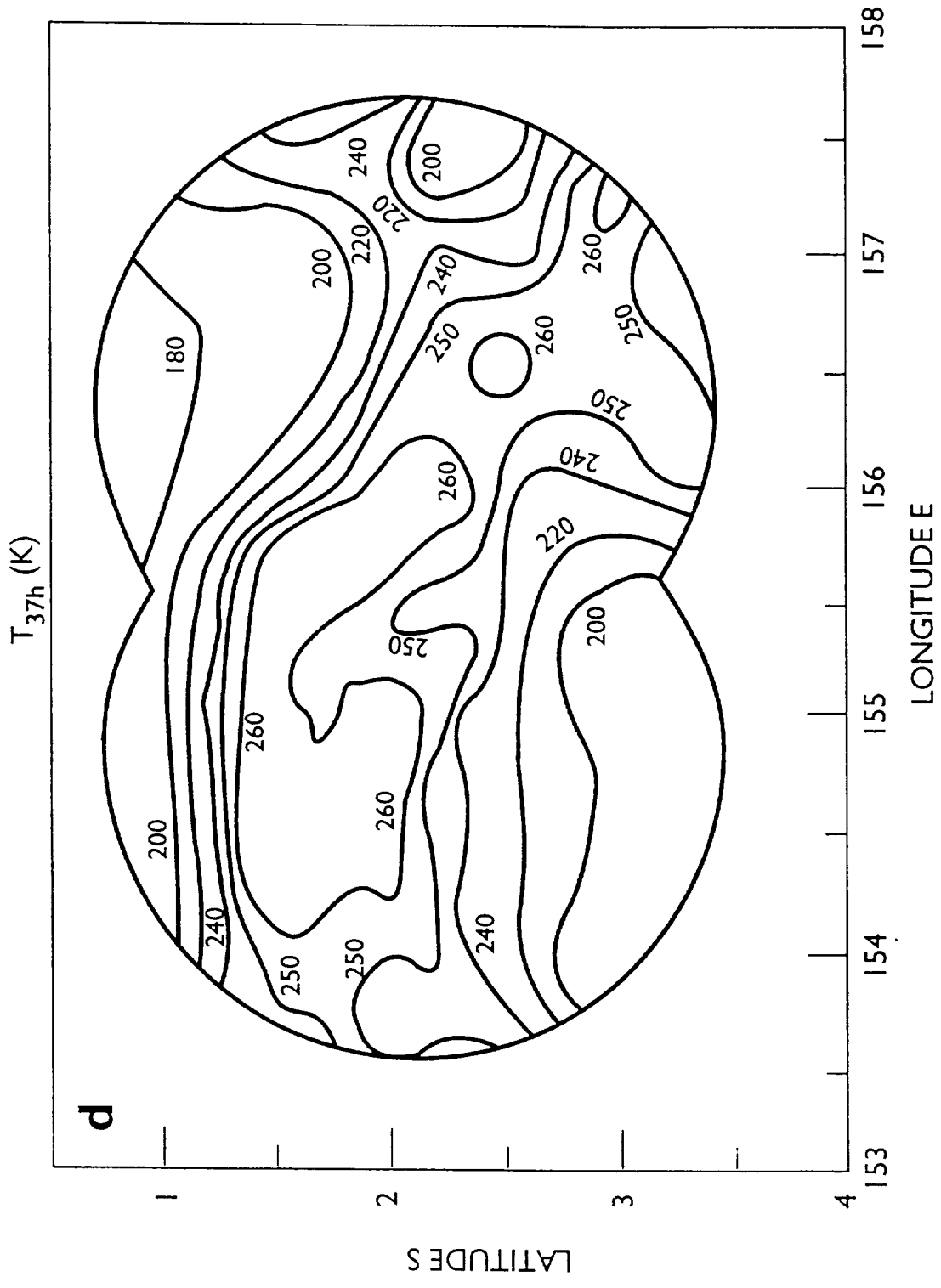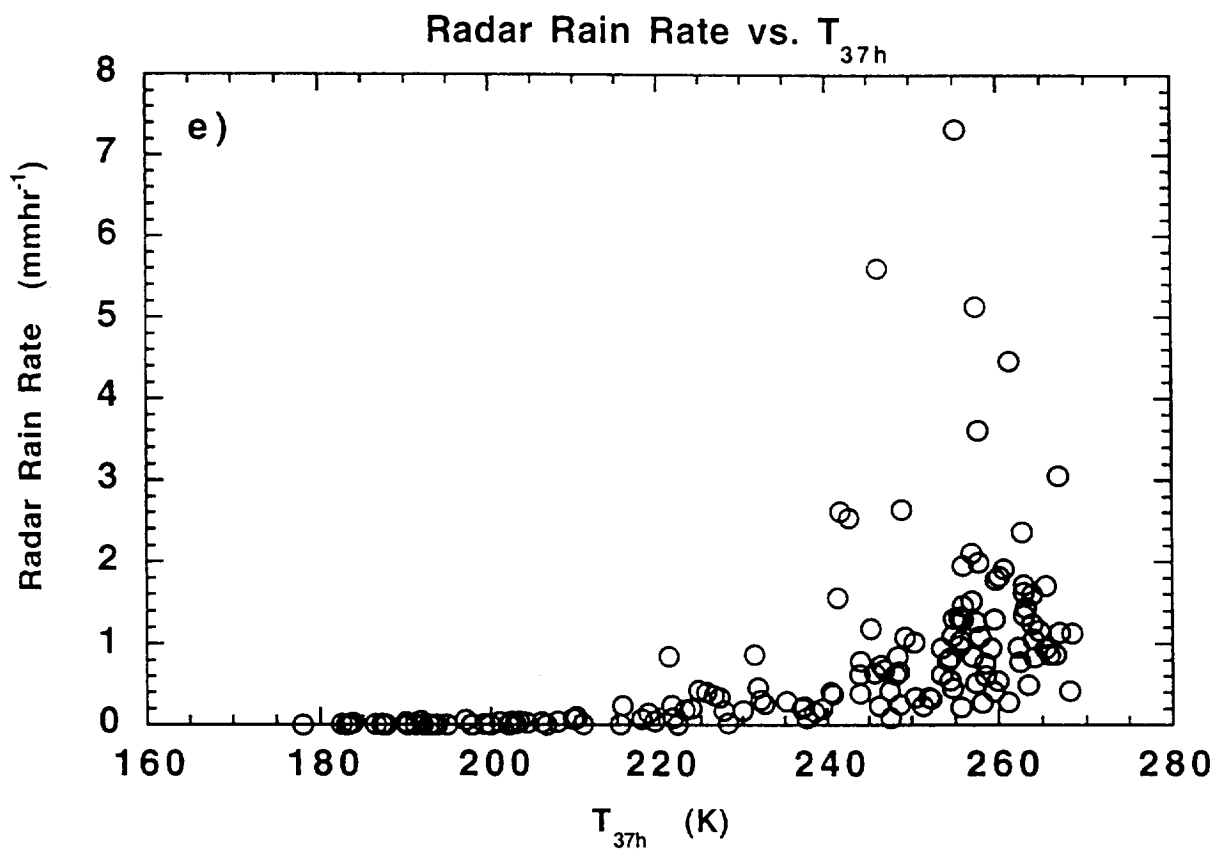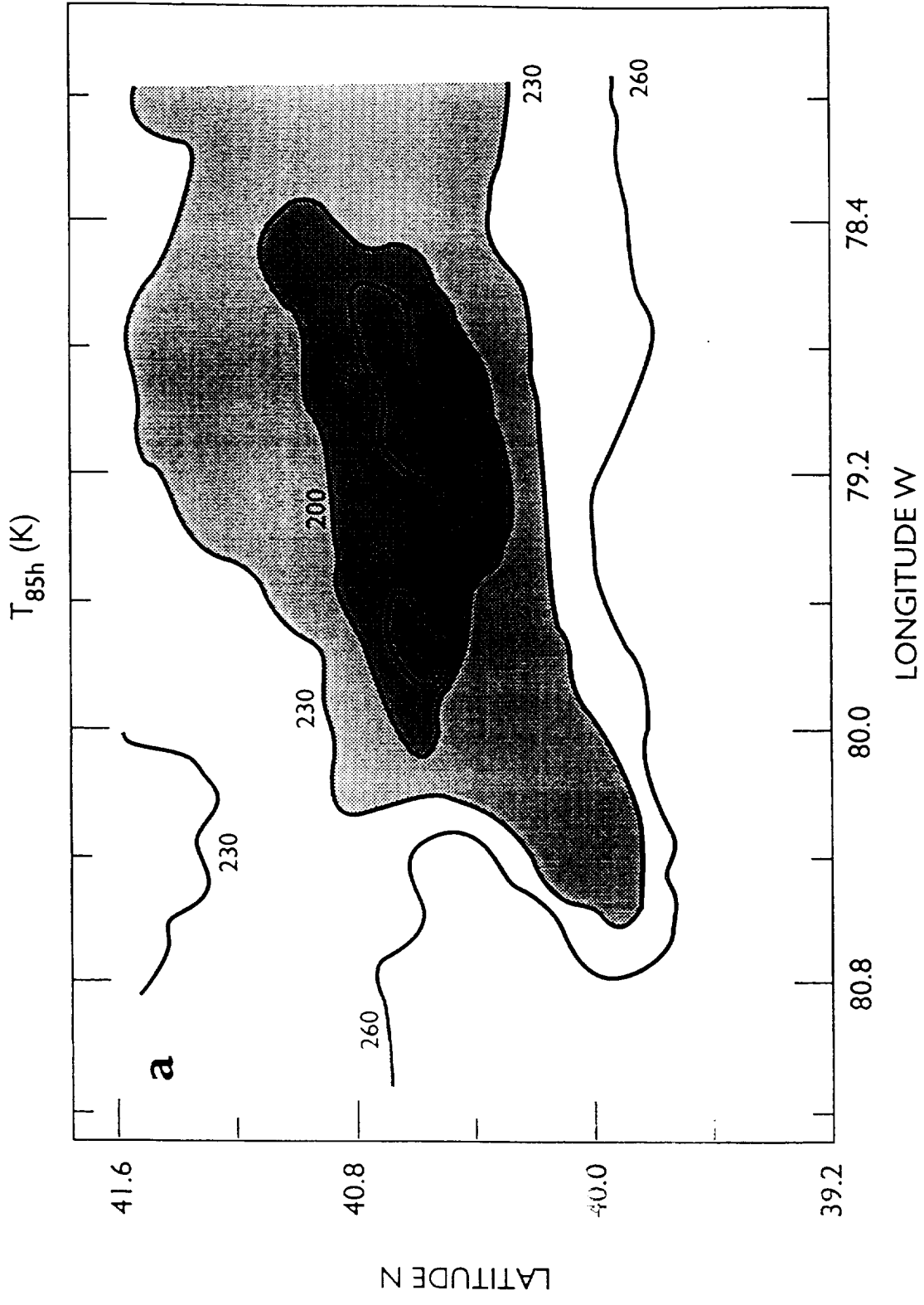
RAIN GAUGE LOCATION & RAIN RATE (mmhr⁻¹)

b

LATITUDE N

LONGITUDE W

Fig 2b

B1099.007

$T_{37h} - T_{85h}$

LONGITUDE W

LATITUDE N

Fig. 2c

B1099005

$T_{19h} - T_{37h}$

d

LONGITUDE W

LATITUDE N

Fig. 2d

B1099 006

Gauge Rain Rate vs. T$_{85h}$

a)

Gauge Rain Rate (mmhr^{-1})

T$_{85h}$

Gauge Rain Rate vs. T$_{85h}$

b)
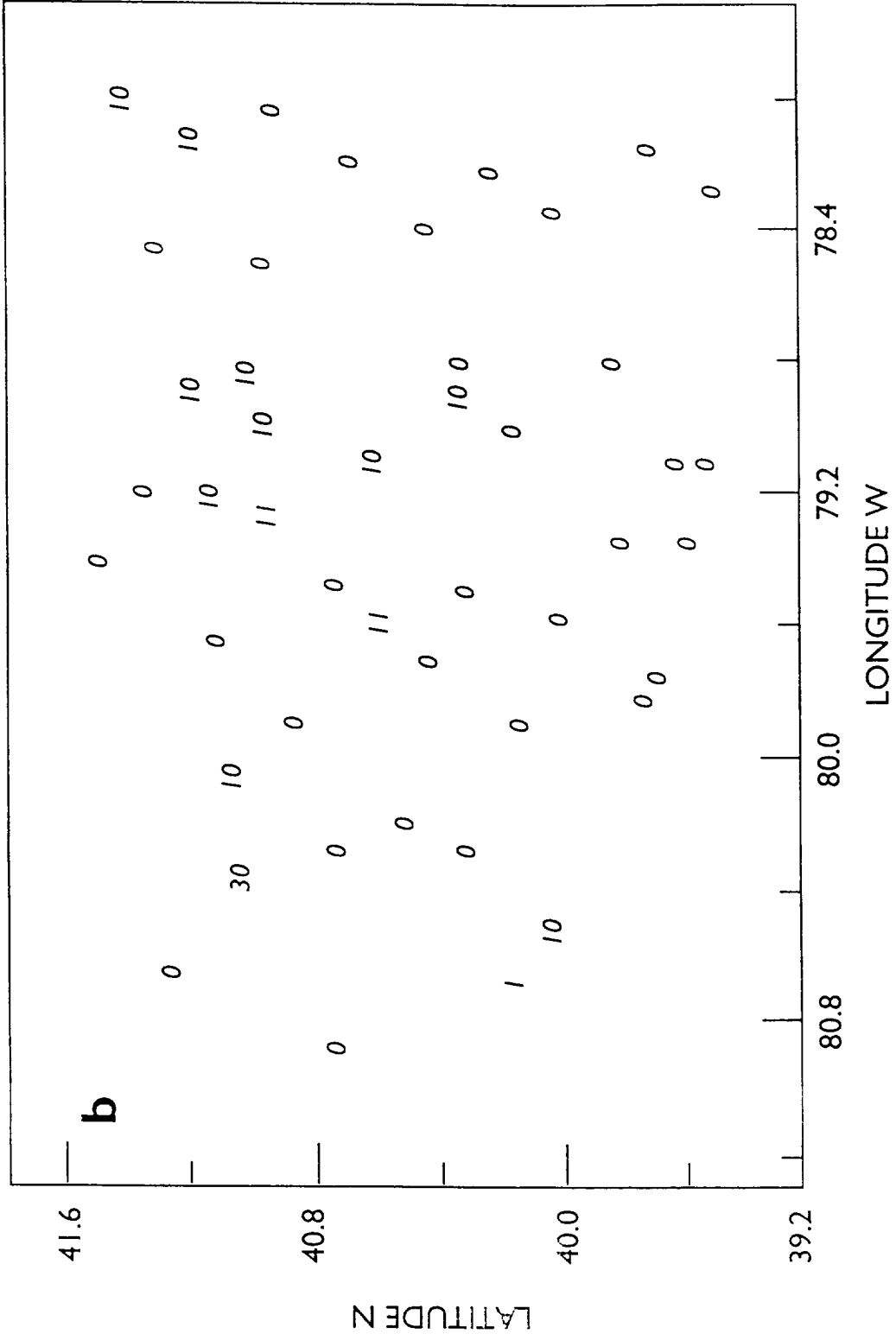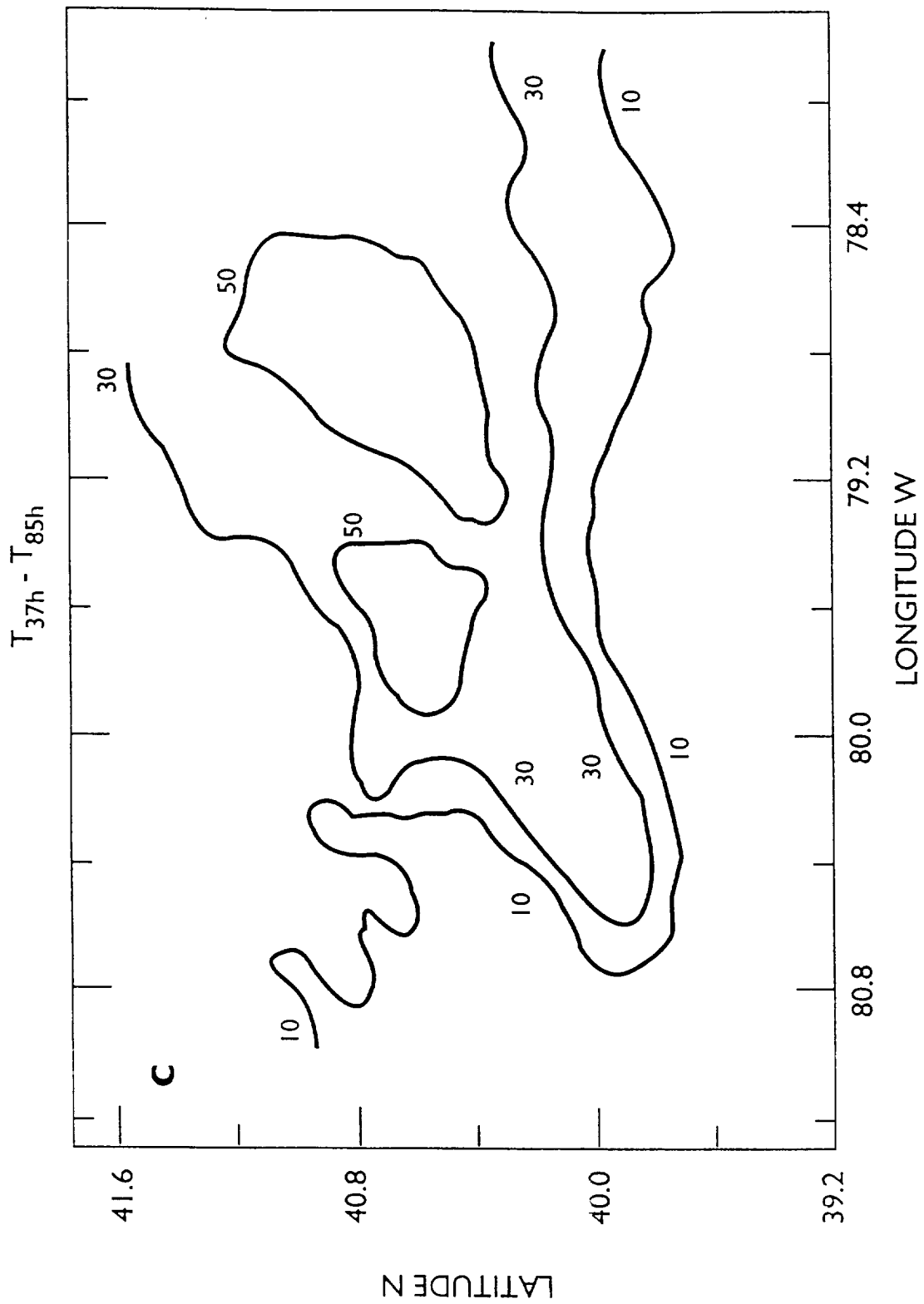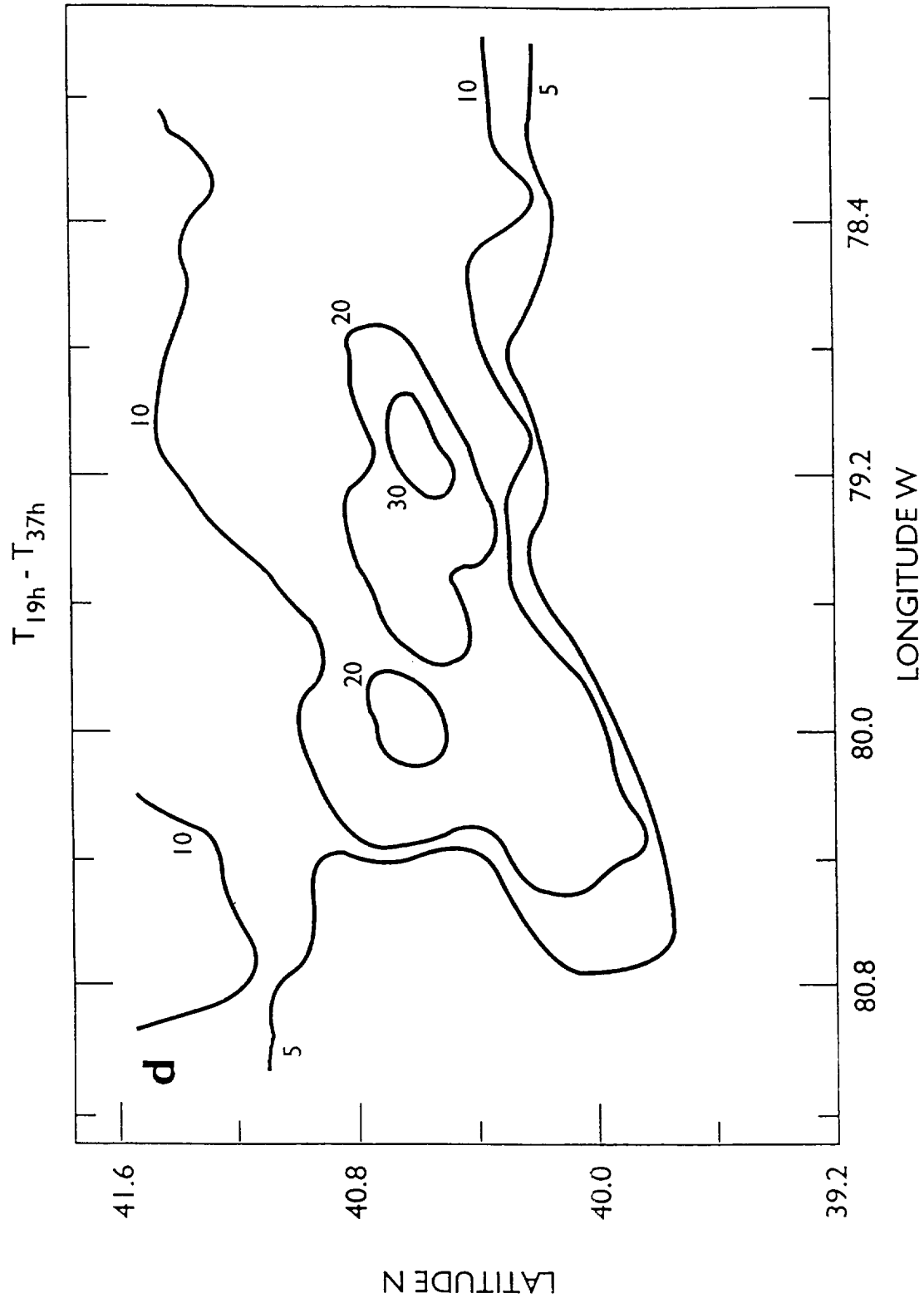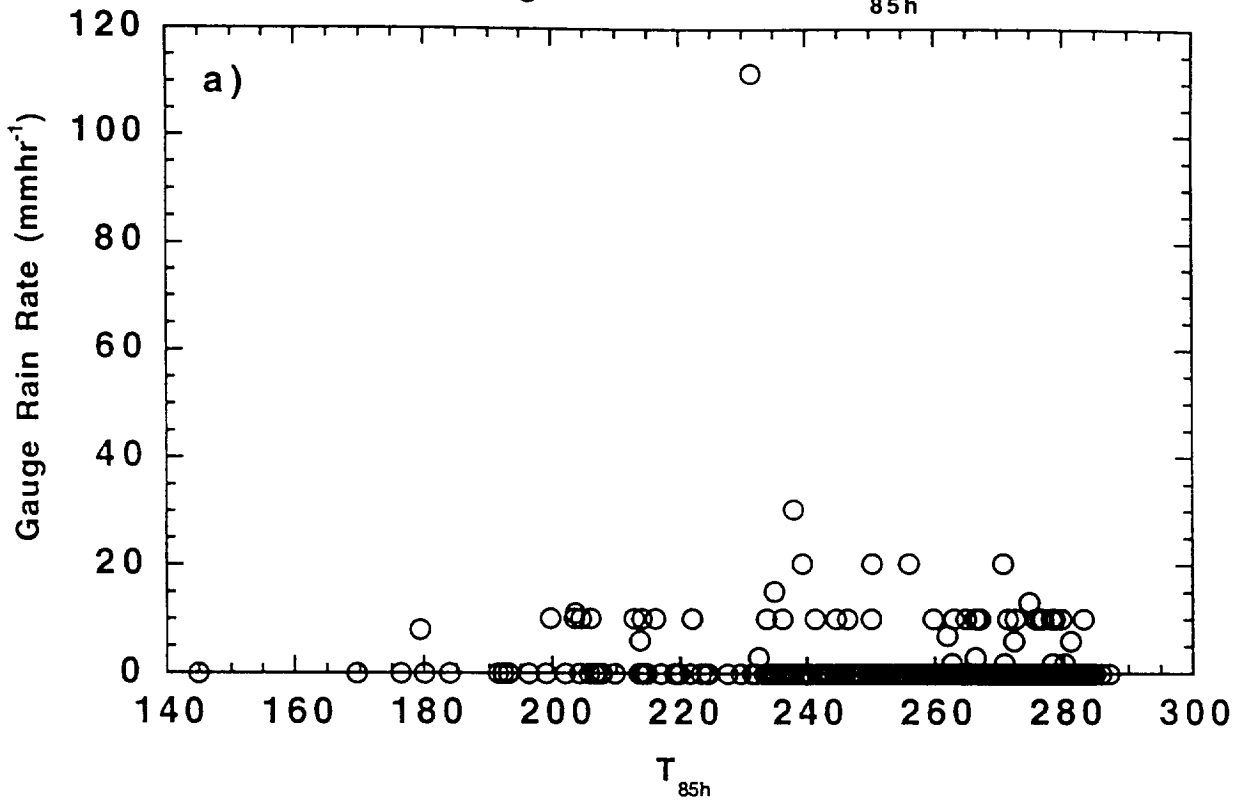
Gauge Rain Rate (mmhr^{-1})
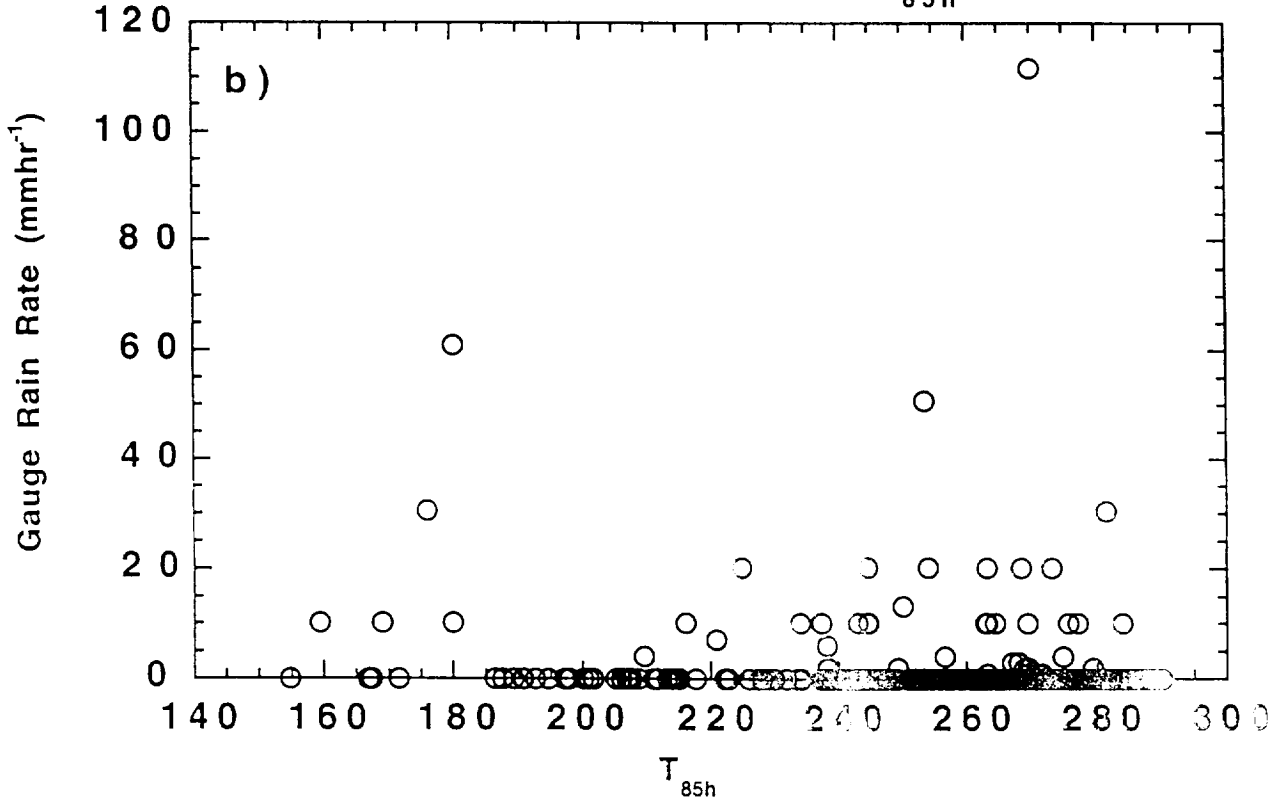
T$_{85h}$

Figs. 3a, 3b

Grid-Box-Average Gauge Rain Rate vs Fractional Rain Area


a) Corr. Coeff. = 0.81

Grid-Box Average Gauge Rain Rate ($mmhr^{-1}$) vs. Fractional Rain Area

Grid-Box-Average Gauge Rain Rate vs. Scattering Depression $(T_{37h} - T_{85h})_{ave}$

b) Corr. Coeff. = 0.46
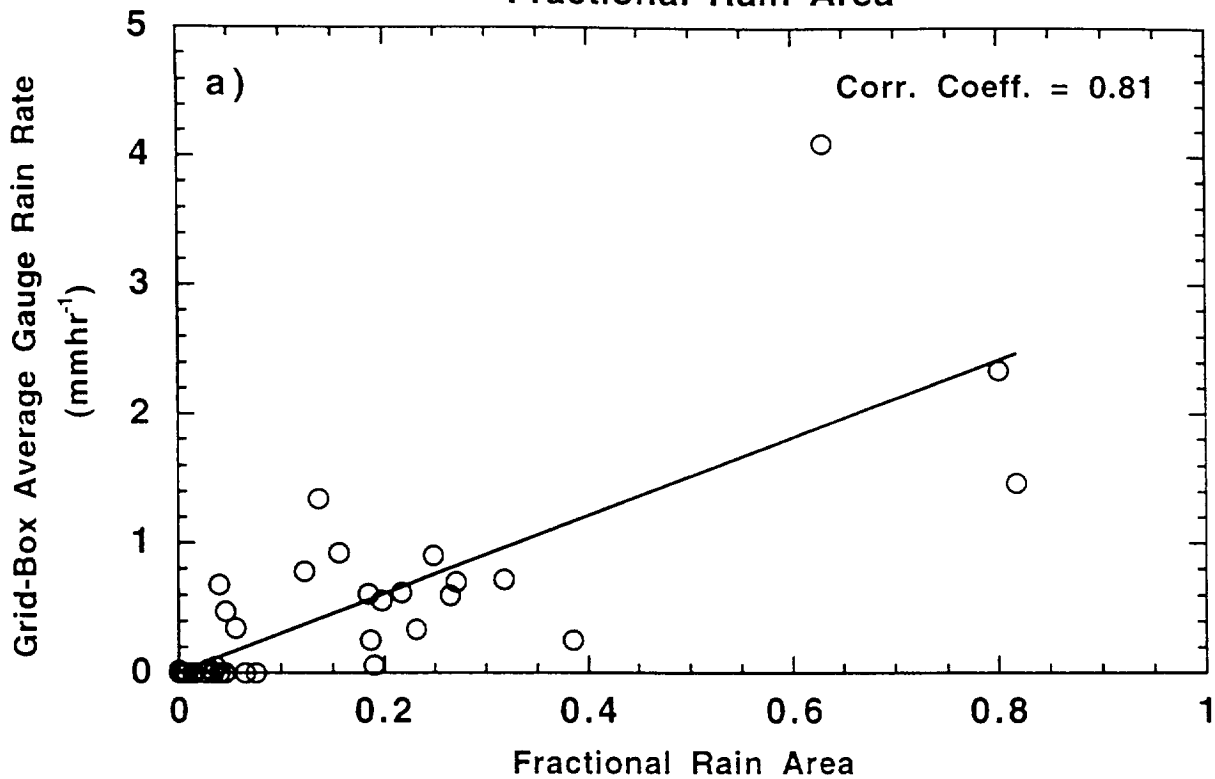
Grid-Box-Average Gauge Rain Rate ($mmhr^{-1}$) vs. $(T_{37h} - T_{85h})_{ave}$ (K)
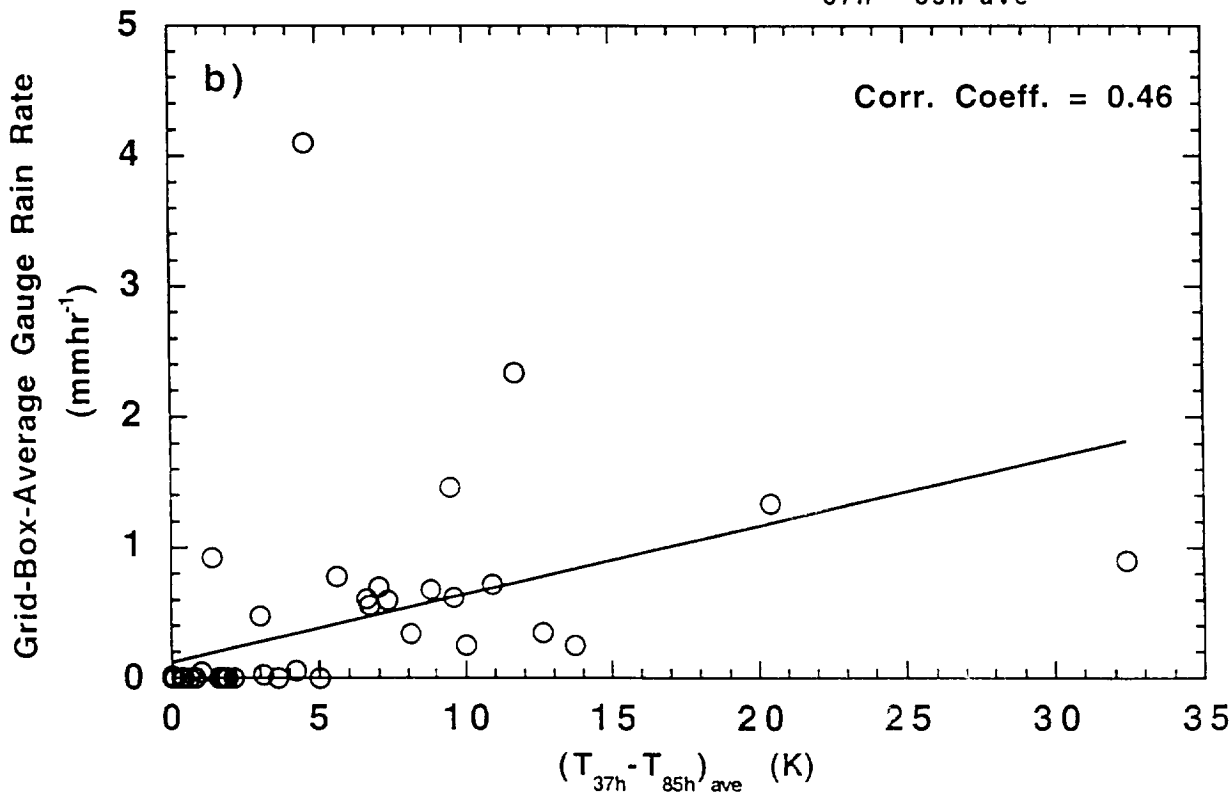
Figs. 4a, 4b

Gauge vs. f_R Algorithm
Grid-Box-Average Rain Rate
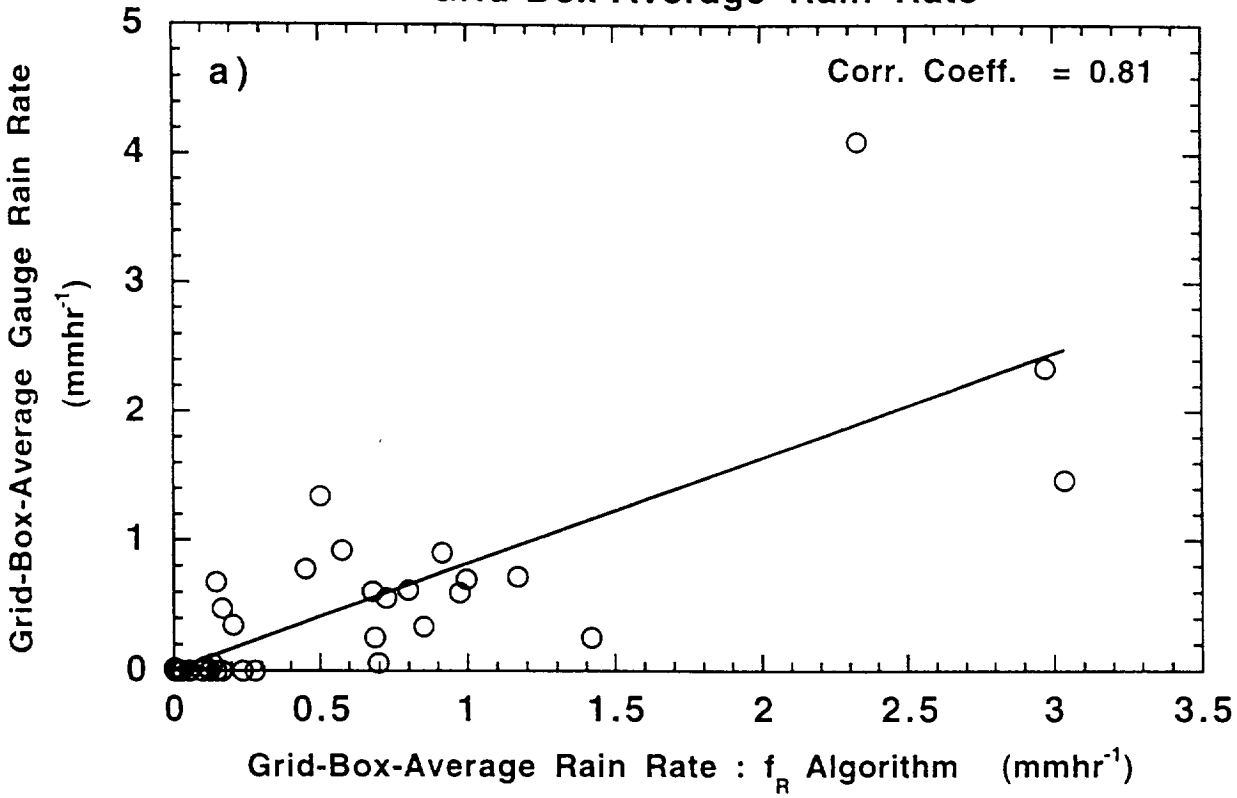
## Gauge vs. $f_R^*(T_{37h}-T_{85h})_{ave}$ Algorithm
Grid-Box-Average Rain Rate
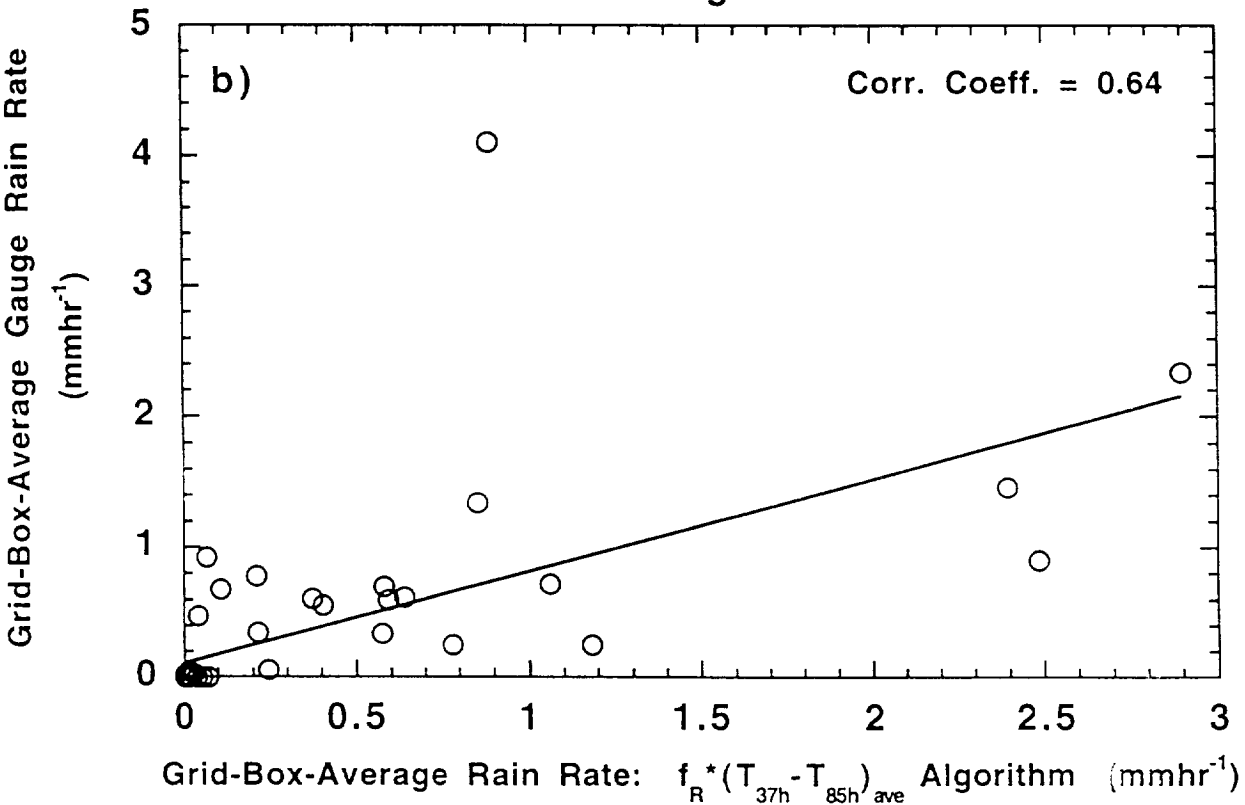
Figs. 5a, 5b

Gauge vs. NASA/GSCAT Algorithm
Grid-Box-Average Rain Rate

a)

Corr. Coeff. = 0.43

Grid-Box-Average Gauge Rain Rate (mmhr^{-1})

Grid-Box-Average Rain Rate: NASA/GSCAT Algorithm (mmhr^{-1})
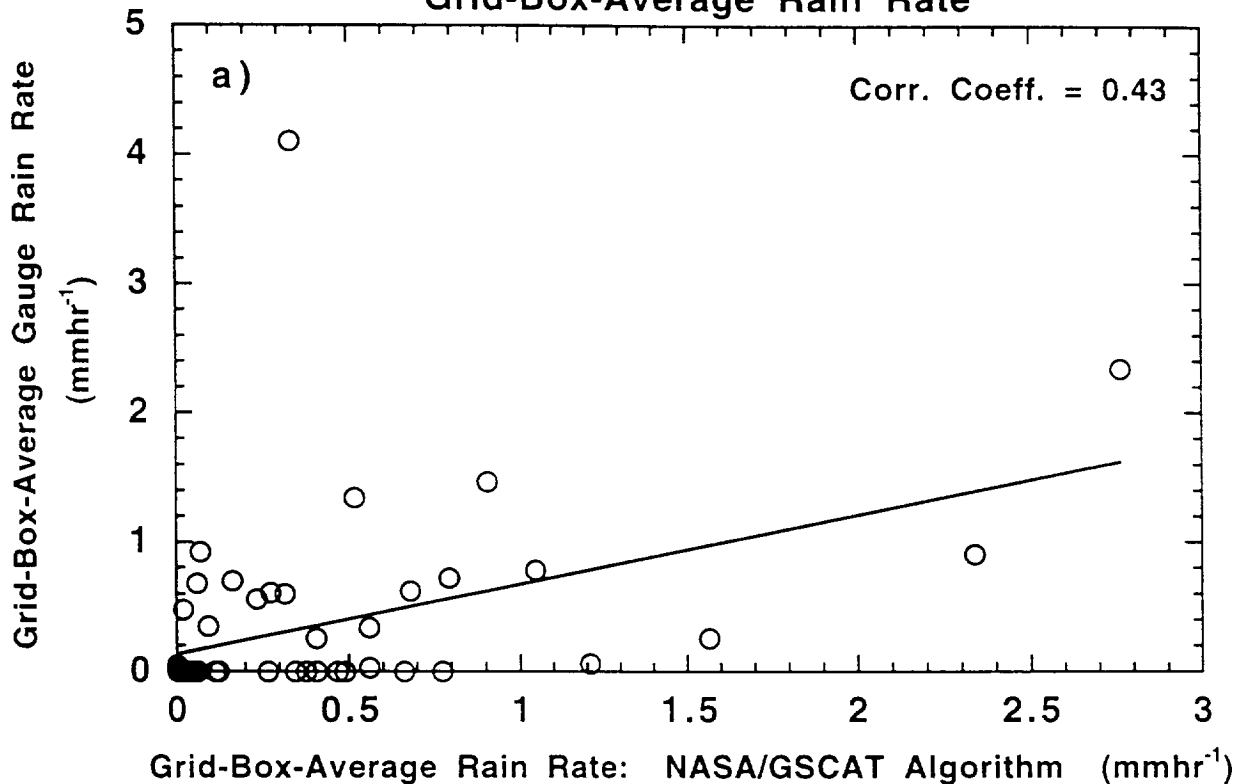
Gauge vs. NOAA/SRL Algorithm
Grid-Box-Average Rain Rate

b)

Corr. Coeff. = 0.37

Grid-Box-Average Gauge Rain Rate (mmhr^{-1})

Grid-Box-Average Rain Rate: NOAA/SRL Algorithm (mmhr^{-1})

Figs. 6a, 6b